Statistical Volume Elements for the Characterization of Angle-Dependent Fracture Strengths in Anisotropic Microcracked Materials

Justin M. Garrard[1]
Department of Mechanical Aerospace
and Biomedical Engineering,
University of Tennessee Space Institute (UTSI)/
Knoxville (UTK),
Tullahoma, TN 37388
e-mail: jgarrard@vols.utk.edu

Reza Abedi
Department of Mechanical Aerospace and
Biomedical Engineering,
University of Tennessee Space Institute (UTSI)/
Knoxville (UTK),
Tullahoma, TN 37388
e-mail: rabedi@utk.edu

Statistical volume elements (SVEs) are used to homogenize fracture strength of rock, based on the microcrack statistics of a real-world Yuen-Long marble sample. The small size of SVEs enables maintaining inhomogeneities in fracture properties with lower computational cost compared to methods that explicitly model microcracks at macroscale. Maintaining inhomogeneity is important to capture realistic fracture patterns in rock as a quasi-brittle material. Uniaxial tensile, uniaxial compressive, and shear strengths are derived for arbitrary angle for loading and orientation of a single crack by using the linear elastic fracture mechanics (LEFM) method and incorporating frictional effects. Mesoscopic fracture strength fields are generated for different strengths and angle of loading by traversing the spatial domain with circular SVEs. Increasing the SVE size smoothens the spatial inhomogeneity and angular anisotropy of homogenized strengths. Spatial and angular covariance functions of the random fields are obtained to demonstrate how fracture strength varies in space and by changing the angle of loading. Two isotropic and anisotropic rock domains are studied and shown to have very different single- and two-point statistics. Macroscopic fracture simulations by an asynchronous spacetime discontinuous Galerkin (aSDG) method demonstrate that most macroscopic cracks for the anisotropic domain are aligned with the weakest strength planes.
[DOI: 10.1115/1.4044607]

1 Introduction

Many common materials used in engineering systems, including rock, concrete, ceramic, and certain composites, are considered quasi-brittle. Understanding their failure mechanisms is vital for using and processing these materials across different size scales. Quasi-brittle materials lack the energy dissipative mechanisms that more ductile materials have [1–3], resulting in a greater importance to understand the distribution of flaws in the microscale, such as microcracks or inclusions. Crack pattern variability for similar sized samples with equivalent loading [4] has been seen due to these microstructural flaws. The *size effect*, wherein the fracture strength decreases as the size of the material sample increases [3,5], is a direct result of these microstructural defects. Therefore, characterizing these networks of microcracks is important to understand the behavior of these materials under loading, as very different fracture patterns [4], ultimate strengths [6,7], and other heterogeneities can be seen for different material samples. Understanding the microstructure of these materials, and its influence on macroscopic fracture, greatly decreases the risk and uncertainty inherent in designs that involve quasi-brittle materials.

Certain material types, such as rock with bedding planes, can contain microstructural defects that are angularly biased, i.e., the microstructure is anisotropic. Depending on the direction of loading, the material strength can be very different. A major increase in risk can be assumed if the engineer only uses a homogeneous, isotropic fracture strength for a given material when designing and modeling an engineering system. To capture these flaws,

implicit or explicit methods may be used to introduce these defects into a given model. *Explicit* methods directly incorporate the microstructure, above certain length scale, into the solution scheme. Some examples are lattice modeling [8] and lattice discrete particle modeling [9], which model the flaws as a particle network connected by springs. Because of the small space and time scales required to properly resolve the microstructural defects in larger structures, explicit methods can be very computationally expensive.

Less computationally intensive *implicit* methods incorporate the overall effect of microstructure in the analysis, but do not directly represent them at the macroscale. An example of an implicit method is Weibull's weakest link method [10,11], which provides a statistical phenomenological characterization of the fracture strength, and has been used successfully by the authors to capture the statistical fracture response of rock in hydraulic fracturing [12], fracture under dynamic compressive loading [13], and in fragmentation studies [14]. While these methods are generally successful in capturing statistical variation for specific properties, they lack the direct connection from the distribution of microstructural defects to macroscopic fracture response.

Therefore, a general method is desired which can link the material microstructure to the meso- and macrostructure that does not require the exorbitant computational costs of explicit methods. To resolve this issue, *homogenization* methods are used to link the material microstructure to the macrostructure by averaging the effect of the microstructure in a volume element (VE). Similar approaches have been used to calibrate certain fracture models, see, for example, Refs. [15–19]. A representative volume element (RVE), also known as a representative elementary volume in rock mechanics, is used in homogenization theories to compute bulk material properties of a composite at the continuum level. The

RVE should be much smaller than the macroscopic domain size so that the homogenized properties of the RVE can be assigned to a point of the continuum domain. Yet, RVEs should be large enough to be representative; that is, for a given homogenized property there is not much variation if larger VEs are used for homogenization. For a macroscopically homogeneous material with ergodic properties, an RVE is defined [20] such that the homogenized properties only vary within a specific range across different realizations of the RVE [21–24]; see also [25,26] for the statistical models that underline the determination of RVE size in preceding references.

A volume element which is smaller than the given size requirements to form a representative volume element is known as a statistical volume element (SVE). These elements may be used to capture the statistical variation in material properties caused by the material microstructure. Multiple SVEs may be used to properly characterize the randomness in material properties. Many studies have been performed to determine how the SVE observation window [27,28], boundary conditions [29], and microstructure defect clustering [30] all effect the given material property statistics. SVEs have been used to capture both the material elastic and fracture properties.

We have used SVEs to homogenize microcracked rocks in Ref. [31] to derive an inhomogeneous yet isotropic field for tensile strength. By computing angle-dependent fracture strengths at the SVE level, anisotropic rocks were homogenized in Ref. [32]. Herein, we extend the work presented in Ref. [32] by using the microcrack statistics of a real-world Yuen-Long marble sample from Ref. [33]. In addition, an index is introduced to determine the anisotropy of homogenized fracture strength fields. Finally, following Ref. [34], spatial and angular covariance functions of the strength fields are used to analyze how the strengths vary in space and as a function of loading direction, respectively.

Once the anisotropy of fracture strength is considered, there are two main approaches to incorporate the anisotropy into a macroscopic continuum model. First, a second-order *microstructure tensor* [35,36] in addition to commonly used invariants of the stress tensor is used to define a general bulk failure criterion. Second, in contrast to the aforementioned bulk failure models, well-known interfacial models such as Mohr–Coulomb or Hoek and Brown [37] are made angle-dependent [38–40] by assigning different tensile strengths or friction coefficients for different angles of loading.

In this work, the latter approach is adopted, such that for any potential angle of loading we characterize different fracture strength parameters. Linear elastic fracture mechanics (LEFM) theory is used to derive angle-dependent uniaxial tensile, uniaxial compressive, and shear strengths. The SVE analysis process and angle-dependent strength formulation are derived in Sec. 2. Then, isotropic and anisotropic microcrack-filled domains are generated using real microcrack distribution statistics from Yuen-Long marble [33] and the statistics of the strength fields are analyzed for isotropic and anisotropic domains. Finally, the asynchronous spacetime Galerkin finite element method [41] is used to analyze the fracture response of these domains with the applied random fracture strength fields.

2 Formulation

This section defines the statistical volume element approach for defining fracture strength with respect to varying loading angle in a quasi-brittle domain containing microcracks. Section 2.1 provides an overview for the anisotropic fracture analysis process in a domain with distributed microcracks using SVEs. The microcrack length and angle distribution will be detailed in Sec. 2.2. Then, Sec. 2.3 describes the process to calculate the mesoscopic angular-dependent fracture strength field. Some useful angle-independent strength measures are introduced in Sec. 2.4. Afterward, a description of the covariance function and its use to determine the correlation of the fracture strength random fields is

provided in Sec. 2.5. Finally, the asynchronous spacetime discontinuous Galerkin (aSDG) method is detailed in Sec. 2.7 for performing macroscopic dynamic fracture simulations within the given quasi-brittle domains.

2.1 Multiscale Anisotropic Fracture Analysis. Figure 1 details the multiscale model that is described in this work. In step one and at the macroscale, an RVE of the given material is considered. In Ref. [33], many samples of Yuen-Long marble were scanned to calculate the statistics of the material microstructure. A 32 mm by 32 mm square domain of Yuen-Long marble was determined to contain a sufficient number of microcracks to be considered representative. The statistics of microcracks demonstrate very low sample to sample variability at this scale. As the size of the RVE decreases, the RVE approaches the SVE regime. The characteristic size of the SVE, l_{SVE}, is smaller than the overall size of the domain of interest and the ratio of the SVE size to the average microcrack length must be small enough that SVE does not approach the RVE limit. As the ratio of l_{SVE} to the average microcrack length approaches infinity, randomness is lost, resulting in a homogeneous material that does not accurately represent the inhomogeneity at the mesoscale due to the existence of microcracks. Several SVE sizes will be studied in Sec. 3 to show this size effect.

Circular SVEs of diameter L_{SVE} are used to transverse the RVE with spacing $S = L_{SVE}/n$, where n is a grid line spacing variable which was chosen such that the entire domain is sampled with sufficient resolution regardless of SVE size. For this paper, n is equal to 5. Within each SVE, the contained microcracks are processed using LEFM principles, as described in Sec. 2.3. A loading P is applied at discrete loading angles, θ, and a field of mesoscopic fracture strength is calculated for each angle; *cf.* step 2 in Fig. 1. In step 3, the calculated strength values are assigned at the center points of the SVEs. In Fig. 1, sample uniaxial tensile strength fields are shown for four different angles of loading. Since the SVE size is at an intermediate level between the representative crack and macroscopic domain sizes, the constructed fields are called *mesoscopic strength fields*. Finally, if desired, dynamic fracture analysis can be performed on the same macroscopic domain shown in step 1 without the explicit representation of microcracks. Instead, by using the mesoscopic fracture strength fields, the computational cost is significantly reduced; still, some level of material inhomogeneity is maintained, which is important for more realistic fracture simulations.

2.2 Microcrack Length and Angle Distributions. Since extensive sampling of rock is difficult or expensive, and detailed microcrack measurements for large domains are scarce, statistical methods are often used to realize microcracked samples that are consistent with the microcrack statistics of the original rock mass. Depending on the method used for realizing samples, different types of statistics of a microcracked domain are used; see Ref. [42] for a few examples. In the *pick-and-place* algorithm, cracks are modeled as discontinuity lines. The distributions of crack center location, length, and angle are sampled for each crack, and a crack with a specific location, length, and angle is inserted in the domain. This process continues until the target crack density ε_0, which is the sum of squares of the microcrack lengths per unit area of the domain, is reached.

While the pick-and-place algorithm can be employed for different microcrack statistics, in this manuscript we use the specific microcrack statistics provided for a Yuen-Long marble sample in Ref. [33], given that all specific descriptors required by this method are experimentally measured and reported therein. Specifically, we employ the statistics of sample S19. The spatial location of the centers of microcracks follows a uniform distribution, as the examined Yuen-Long marble is macroscopically homogeneous. A power-law distribution is used, and experimentally verified, to represent the distribution of crack length in Ref. [33]. In
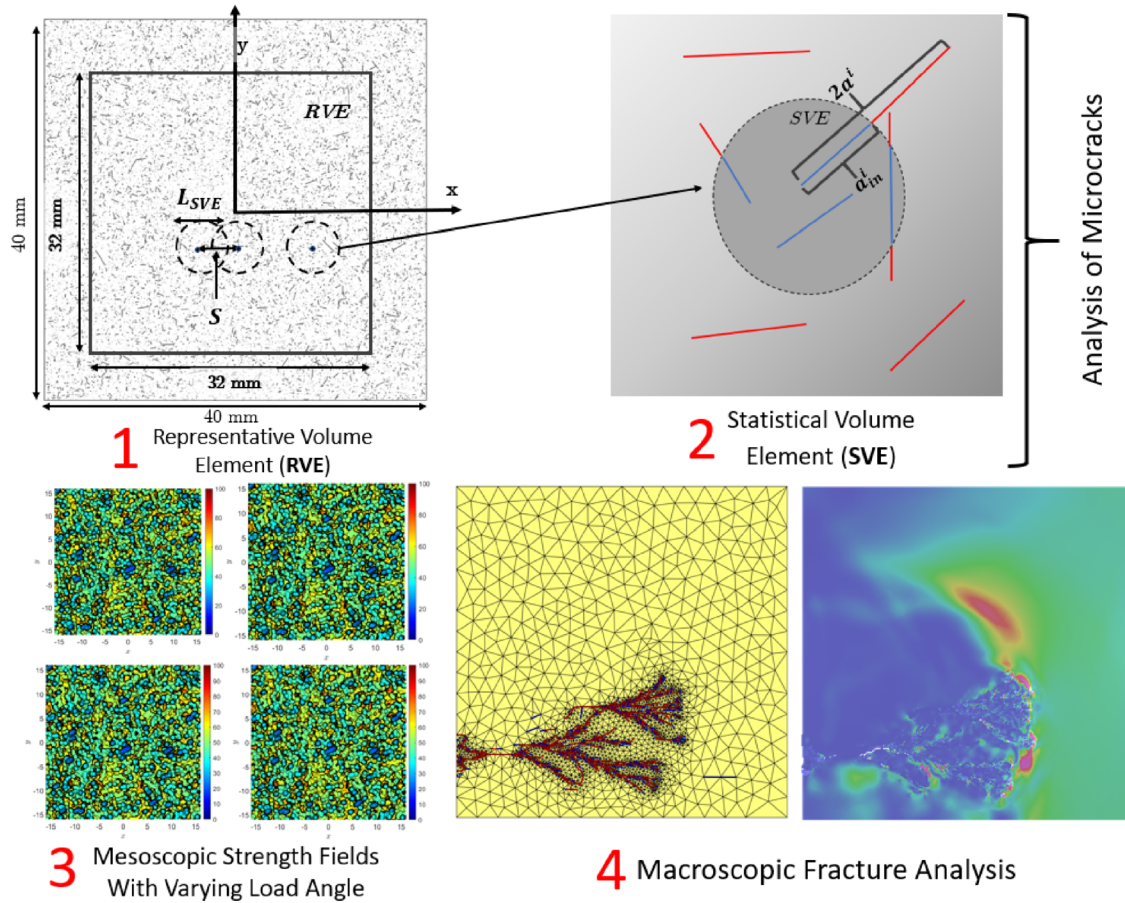
Fig. 1   A multiscale model for anisotropic fracture analysis of microcracked rock

fact, as discussed in Ref. [43], field observations indicate that crack length often follows a power law distribution in rock. For the power-law distribution a minimum value (crack half-length) a' is assigned to ensure the cumulative distribution function to be finite and take the value of one for infinite crack half-length; cf. Eq. (2) below. The cumulative distribution for half-cracks longer than a' for an elemental volume V_0 is defined as

$$g(a) = \left(\frac{q^*}{a}\right)^z \tag{1}$$

where $q*$ and Cauchy distribution exponent $z > 1$ are the parameters of the power distribution, subject to the condition

$$V_0 \int_{a'}^{\infty} g(a)da = 1 \tag{2}$$

To ensure this equality, the lower integration limit, a' is defined by

$$a' = \left[\frac{(q^*)^z V_0}{z - 1}\right]^{\frac{1}{z-1}} \tag{3}$$

The specific model values for sample S19 are reported in Sec. 3 and used to generate new random crack fields consistent with S19 microcrack length statistics.

The S19 rock sample from Ref. [33] is isotropic and crack angle follows a uniform distribution. We will use this actual angle distribution to realize a macroscopically *isotropic rock domain*. Since one objective of this study is relating the angle distribution of microcracks to anisotropy of the mesoscopically homogenized fracture strength fields, we create a second macroscopically

anisotropic rock domain where the angle distribution is intentionally nonuniform. A triangular distribution with a peak at $\theta_c = 30$ deg and a range of $\theta_c = 25$–35 deg is used for this synthetic crack angle distribution. The final parameter for defining the microcrack domain is the crack density, where for both rock domains, the crack density of $\varepsilon_0 = 0.243$ of sample S19 is used.

It is noted that the statistics of microcracks plays a crucial role in the homogenized strengths at the mesoscale and macroscopic fracture properties. For example, we have demonstrated that by changing the shape of microcrack length distribution, while keeping the mean length fixed, macroscopic fracture strength can change by a factor of three [44]. Our focus in the remainder of the manuscript will be on the effect of statistics of microcracks on mesoscopic and macroscopic response, rather than validation of the macroscopic response with experimental results. Specific attention is directed to angular dependency of properties at different scales.

2.3   Fracture Strength Calculations. Within the SVE, the fracture strength of every microcrack intersecting the element is calculated. As detailed previously, a circular SVE observation window was selected. Cracks that are both completely encircled or only partially intersecting an SVE are considered. For SVEs which contain no microcracks, a maximum fracture strength is assigned based on a crack of minimum length. As all of the intersecting cracks fracture strengths are calculated, the minimum fracture strength is retained and assigned to the center point of the SVE, resulting in a mesh of fracture strengths with uniform spacing in both horizontal and vertical directions. Each mesh point contains a vector of angular-dependent fracture strengths, i.e., the fracture strength calculated for each discrete loading angle.

It is noted that a few SVEs may contain no cracks. For these SVEs, a maximum fracture strength is assigned based on a crack

of minimum length to avoid having an infinite strength. This minimum length is twice the value of minimum allowable half-length crack a' for the power law distribution in Eq. (3). For the homogenization to be valid, the SVE size should be chosen large enough such that the majority of SVEs are representative of rock microstructure, in that they contain a sufficient number of microcracks. This size depends on the (length) distribution of microcracks and crack density. If the SVE size is too small, the maximum strength based on the minimum crack length is assigned to many SVEs. However, in this paper, the SVE sizes are chosen large enough that even for the smallest SVE size, very few SVEs contain no cracks.

For a crack of half-length a, the strength is calculated using LEFM principles. There are three assumptions in calculating fracture strengths. First, the interaction of microcracks is not taken into account. Second, for the microcracks that intersect the boundary of the SVE, the geometric mean of the total microcrack length and the part that is inside the SVE is used for its effective length in LEFM calculations; that is, $a_{\mathrm{eff}}^i = \sqrt{a^i a_{\mathrm{in}}^i}$ for microcrack number i in Fig. 1. Third, as will be described below, the principle of maximum energy release rate (MERR) [45] is used to compute fracture strength of individual cracks.

Figure 2 shows the schematic of a single crack with effective half length a_{eff} with angle θ_c and local coordinate system (x', y'). The global Cartesian coordinate system is (X, Y). We are interested in computing various fracture strengths for a loading angle of θ. As shown, the coordinate system (x, y) for far field loading is at angle θ with respect to the global coordinate system (X, Y). Thus, the relative angle of the crack with respect to x is $\theta_d := \theta_c - \theta$. For computing fracture strengths at angle θ, in-plane stresses are applied in the (x, y) coordinate system. To use LEFM theory, we need to transfer these stresses to the (x', y') coordinate system. This is achieved by Mohr circle transformation of the in-plane components of the stress tensor between the two coordinate systems

$$\sigma_{x'x'} = \sigma_{xx} \cos^2\theta_d + \sigma_{yy} \sin^2\theta_d + \sigma_{xy} \sin 2\theta_d \qquad (4a)$$

$$\sigma_{y'y'} = \sigma_{xx} \sin^2\theta_d + \sigma_{yy} \cos^2\theta_d - \sigma_{xy} \sin 2\theta_d \qquad (4b)$$

$$\sigma_{x'y'} = -\sin 2\theta_d \frac{\sigma_{xx} - \sigma_{yy}}{2} + \sigma_{xy} \cos 2\theta_d \qquad (4c)$$

The strengths for angle θ correspond to the following stress tensors $\boldsymbol{\sigma} = (\sigma_{xx}, \sigma_{yy}, \sigma_{xy})$ in (x, y) coordinate system:

$$\boldsymbol{\sigma} := (s_{\mathrm{NH}}, s_{\mathrm{NH}}, 0) \quad \text{hydrostatic tensile strength } s_{\mathrm{NH}} \qquad (5a)$$

$$\boldsymbol{\sigma} := (0, s_N(\theta), 0) \quad \text{uniaxial tensile strength } s_N \qquad (5b)$$

$$\boldsymbol{\sigma} := (0, -s_C(\theta), 0) \quad \text{uniaxial compressive strength } s_C \qquad (5c)$$

$$\boldsymbol{\sigma} := (0, 0, s_S(\theta)) \quad \text{shear strength } s_S \qquad (5d)$$

where as mentioned $s_N(\theta)$, $s_C(\theta)$, and $s_S(\theta)$ are positive uniaxial tensile, uniaxial compressive, and shear strengths at angle θ. Note that there is no argument of loading direction for hydrostatic tensile strength since it corresponds to equal principle stresses s_{NH} for all angles of loading. We also observe that uniaxial tensile strength at angle θ corresponds to $\boldsymbol{\sigma} = (0, s_N(\theta), 0)$ rather than $(s_N(\theta), 0, 0)$; for this strength at angle θ, we apply a tensile stress normal to the direction of a hypothetical fracture line with angle θ. This corresponds to only σ_{yy} nonzero in Fig. 2. Finally in Eq. (5), the form of any of the loadings for angle θ is known, but the factor of stress tensor for which the crack with $2a_{\mathrm{eff}}$ at angle θ_c satisfies an LEFM fracture criterion corresponds to the magnitude of the strength.

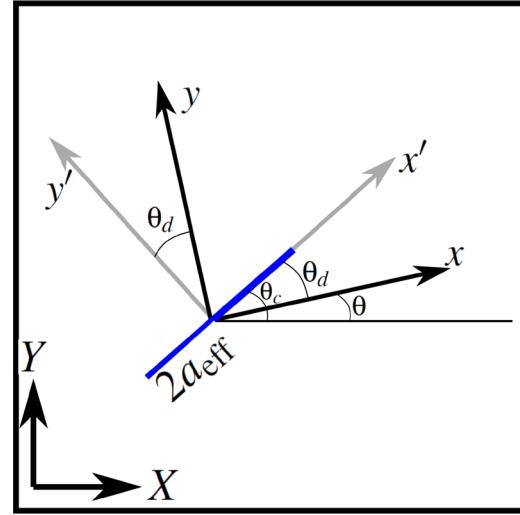The resolvent components of traction $\mathbf{t} = (t_n, t_s)$ acting on the crack plane are

Fig. 2 Crack angle θ_c and loading angle θ

$$t_n = \sigma_{y'y'} \qquad (6a)$$

$$t_s = |\sigma_{x'y'}| - k\langle -t_n \rangle_+ \qquad (6b)$$

where t_n and t_s are the normal and shear components of $\mathbf{t}$, k is the friction coefficient, and $\langle . \rangle_+$ is the Macaulay positive operator. The reason that in Eq. (6b) the positive operator acts on $-t_n$, is that for the shear stress to induce mode II fracture, the far field shear stress $\sigma_{x'y'}$ must be greater than the friction traction $k\langle -t_n \rangle_+$. When under tensile loading, i.e., when $t_n \geq 0$, friction is zero ($k\langle -t_n \rangle_+ = 0$). We model the crack in Fig. 2 in isolation undergoing far field normal stress t_n, corresponding to mode I fracture if $t_n > 0$. The resolvent shear stress t_s results in a mode II stress intensity factor (SIF) if acting shear stress $|\sigma_{x'y'}|$ can overcome friction $k\langle -t_n \rangle_+$, i.e., when $t_s > 0$. Thus, modes I and II SIFs at the crack tips are

$$K_I = \frac{\langle t_n \rangle_+}{\sqrt{\pi a_{\mathrm{eff}}}} \qquad (7a)$$

$$K_{II} = \frac{\langle t_s \rangle_+}{\sqrt{\pi a_{\mathrm{eff}}}} \qquad (7b)$$

There are several criteria such as maximum circumferential stress criterion, MERR, and minimum strain energy density that can be used to determine whether K_I and K_{II} are large enough to result in propagation at the tips of the crack and at what direction relative to the crack the extension will propagate. For the MERR criterion, to investigate crack propagation at a potential kink angle ψ relative to crack direction, stress intensity factors at the tip of the kink crack extension, $K_I(\psi)$ and $K_{II}(\psi)$, need to be computed from K_I and K_{II} in Eq. (7) [46]. The crack extends in a direction ψ for which the energy release rate in terms of $K_I(\psi)$ and $K_{II}(\psi)$ is maximum and exceeds the fracture toughness of material [45]. One can show that the corresponding failure criterion in terms of K_I and K_{II} can very accurately be approximated by

$$K_I^2 + K_{II}^2 = K_c^2 \qquad (8)$$

where K_c is the critical mode I SIF. For plane stress condition, i.e., for samples with small thickness B, tri-axial stress state is less pronounced than plane strain condition. Thus, K_c is larger than K_{Ic}, its corresponding value for plane stress condition. In general, K_c can be obtained from B and K_{Ic} [47]. While MERR criterion is slightly less conservative than maximum circumferential stress criterion and minimum strain energy density criteria, the form of the approximate relation (8) greatly simplifies the determination

of fracture strengths for a crack with relative angle θ_c to the loading direction.

The process for computing any of the fracture strengths s_{NH}, $s_N(\theta)$, $s_C(\theta)$, and $s_S(\theta)$ is summarized as followed. First, relative crack angle is computed from $\theta_d = \theta - \theta_c$. Second, the stress tensor in (x, y) coordinate system corresponding to the given strength is chosen from Eq. (5). Third, the stress tensor is transferred to (x', y') coordinate system from Eq. (4). Fourth, resolvent traction components t_n and t_s are computed from Eq. (6). Fifth, SIFs K_I and K_{II} are computed from Eq. (7). Finally, the magnitude of the given strength, e.g., $s_N(\theta)$, is computed such that the failure criterion (8) is satisfied. As will be discussed later, for certain strengths and angles θ_d, one or both of t_n and t_s are negative and Eq. (8) cannot be satisfied for any magnitude of loading; that is, the given angle-dependent strength is infinite.

Following this process for the four different strengths, the angle-dependent strengths are obtained as:

$$\frac{s_{NH}\sqrt{\pi a_{\mathrm{eff}}}}{K_c} = 1 \tag{9a}$$

$$\frac{s_N(\theta)\sqrt{\pi a_{\mathrm{eff}}}}{K_c} = \frac{1}{\cos\theta_d} \tag{9b}$$

$$\frac{s_C(\theta)\sqrt{\pi a_{\mathrm{eff}}}}{K_c} = \begin{cases} \dfrac{1}{-\cos\theta_d(\sin\theta_d + k\cos\theta_d)}, & -\dfrac{\pi}{2} < \theta_d < -\phi \\ \infty, & -\phi < \theta_d < \phi \\ \dfrac{1}{\cos\theta_d(\sin\theta_d - k\cos\theta_d)}, & -\phi < \theta_d < \dfrac{\pi}{2} \end{cases} \tag{9c}$$

$$\frac{s_S(\theta)\sqrt{\pi a_{\mathrm{eff}}}}{K_c} = \begin{cases} 1, & -\dfrac{\pi}{2} < \theta_d < 0 \\ \dfrac{1}{\cos 2\theta_d - k\sin 2\theta_d}, & 0 < \theta_d < \left(\dfrac{\pi}{4} - \dfrac{\phi}{2}\right) \\ \infty, & \left(\dfrac{\pi}{4} - \dfrac{\phi}{2}\right) < \theta_d < \left(\dfrac{\pi}{4} + \dfrac{\phi}{2}\right) \\ \dfrac{1}{-\cos 2\theta_d - k\sin 2\theta_d}, & \left(\dfrac{\pi}{4} + \dfrac{\phi}{2}\right) < \theta_d < \dfrac{\pi}{2} \end{cases} \tag{9d}$$

where $\phi := \tan^{-1}(k)$ is the friction angle. Also, note that the relative crack angle θ_d is taken in $(-\pi/2, \pi/2)$, given that shifts of π in crack angle do not change the problem description in Fig. 2. Based on Eq. (9a), the maximum (hydrostatic tensile strength, NH), corresponding on minimum half-length crack a' is $S_{\max} = K_c/\sqrt{\pi a'}$.

The fracture strengths in Eq. (9) are shown in Fig. 3 for $k = 0.3$. As expected, the hydrostatic tensile strength is angle-independent and takes the value $K_c/\sqrt{\pi a_{\mathrm{eff}}}$. The uniaxial tensile strength takes the lowest value when the loading is normal to the crack, that is, for $\theta_d = 0$. As $|\theta_d| \to \pi/2$, a much higher normal stress in y' is needed to result in crack propagation through Eq. (8). For the compressive strength, the resolvent t_n is always negative and the friction term in Eq. (6b) is nonzero. Under this loading, crack can propagate only in mode II if $|t_s| \geq 0$; cf. Eq. (7b). For relative crack angles $|\theta_d| \leq \phi$, the friction traction $k\langle -t_n\rangle$ is higher than $|\sigma_{x'y'}|$. Consequently, crack surfaces cannot slip and have the excess shear stress resulting in mode II crack propagation. For $|\theta_d| > \phi$, slip can occur. The maximum uniaxial compressive strength of $2\cos\phi K_c/(1 - \sin(\phi)\sqrt{\pi a_{\mathrm{eff}}}$ is achieved for $|\theta_d| = \phi/2 + \pi/4$. As $|\theta_d| \to \pi/2$, $s_C(\theta)$ tends to infinity.

The only strength whose dependency is not even with respect to θ_d is $s_S(\theta)$. When $\theta_d = -\pi/2$, the stress state (5d) results

in $\sigma_{y'y'} = s_S(\theta_d = -\pi/4)$ and $\sigma_{x'y'} = 0$ in Eqs. (4b and 4c). Thus, $t_n = s_S(\theta_d = -\pi/4)$ and $t_s = 0$ in Eq. (6) and the crack is in pure mode I; cf. Eq. (7). On the other hand, for $\theta_d = \pi/4$ we obtain $t_n = -s_S(\theta_d = \pi/4)$ and $t_s = 0$. That is, $\theta_d = -\pi/4$ and $\pi/4$ correspond to pure tension and compression on crack surfaces. Clearly, in the former case, the strength is equal to uniaxial strength, and in the latter case, the crack cannot propagate. This explains the nonsymmetric dependency of s_S on θ_d. In short, for $\theta_d < 0$, the resultant t_n is positive and crack can propagate in mixed mode. For $\theta_d > 0$, $t_n < 0$ and crack can only propagate when resolvent shear stress is positive, that is tangential stress $\sigma_{x'y'}$ is larger than friction term $k\langle -t_n\rangle_+$ in Eq. (6b). This occurs for $|\theta_d - \pi/4| > \phi/2$.

For a given SVE, the hydrostatic tensile strength S_{NH}, and angle-dependent uniaxial normal $S_N(\theta)$, uniaxial compressive $S_C(\theta)$, and shear $S_S(\theta)$ strengths are defined as

$$S_\alpha(\theta) = \min_{i\in\mathcal{I}_{SVE}} s_\alpha^i(\theta) \tag{10}$$

where α refers to one of the strength modes NH, N, C, and S. The minimum of strength is taken over microcracks with index i over $\mathcal{I}_{SVE}$, the set of all microcracks that are in or intersect the SVE; cf. Fig. 1(b). That is, for a given loading direction and strength type, the SVE takes the minimum of the corresponding strength of all the cracks that interact with the SVE.

There are three assumptions in using Eq. (10) as follows. First, the value of $S_\alpha(\theta)$ is capped by $S_{\max}$, the maximum fracture strength based on the value of a'. Since in Eq. (9) some of these strengths are infinite or tend to infinity, depending on the angle θ_d, for some SVEs $S_\alpha(\theta)$ may take a very large value even if it contains some microcracks. Using the maximum value $S_{\max}$ basically denotes an infinite value for $S_\alpha(\theta)$, corresponding to a situation that none of the microcracks can propagate for the given angle of loading. This is specifically relevant to the anisotropic rock domain as discussed in Sec. 3.2. Second, it is assumed that all these microcracks are effectively in an infinite domain. This is a reasonable assumption for the majority of SVEs, if the SVE size is sufficiently smaller than the macroscopic domain size. Third, microcrack interaction is not taken into account. Generally, microcrack interaction reduces the strength. In many studies, crack interaction is taken into account by reducing the strength through a nonincreasing function of crack density in the form $y(\varepsilon_0)$; see, for example, Refs. [33] and [48]. No microcrack interaction model is employed in this study. This is because we are more interested in spatial variation of strengths, averaged by using SVEs, rather than their absolute values. Moreover, these crack interaction models often can analytically be computed only for simplistic microcrack distributions such as periodic array of parallel cracks with the same size. We believe that full-scale finite element analysis should be employed to accurately model crack
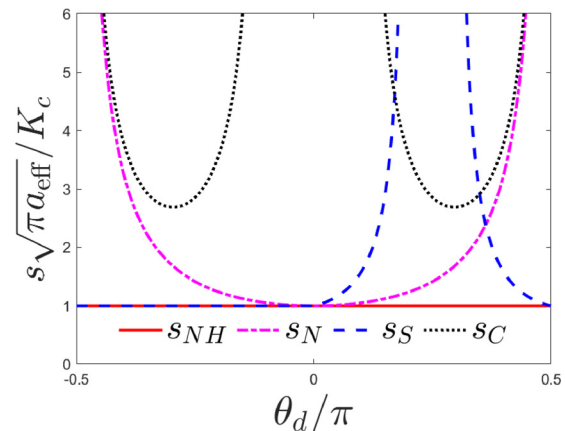

Fig. 3 Different fracture strengths for the crack in Fig. 2 as a function of relative crack angle θ_d for $k = 0.3$

interaction for more general distribution of microcracks. However, the computational cost of this approach is prohibitive herein, given that an extremely large number of SVEs are analyzed to study the statistics of homogenized strengths.

2.4 Angle-Dependency of Fracture Strength. For an SVE, fracture strengths $S_\alpha(\theta)$, for $\alpha \in \{NH, N, C, S\}$, are angle-dependent. Accordingly, we can define the following angle-independent measures for an SVE:

$$m(S_\alpha) = \min_{\theta \in [0,\pi]} S_\alpha(\theta) \tag{11a}$$

$$\bar{S}_\alpha = \text{mean}_{\theta \in [0,\pi]} S_\alpha(\theta) \tag{11b}$$

$$A_\alpha = \frac{\bar{S}_\alpha}{\varsigma_{\theta \in [0,\pi]} S_\alpha} \tag{11c}$$

where ς stands for standard deviation. If angular dependency of fracture strength is not very high and there is not a specific bias with respect to a given angle, for example, rocks with bedding plane, the minimum SVE strength $m(S_\alpha)$ over all angles of loading, can be considered as a reasonable angle-independent fracture strength for the SVE. The mean SVE strength, $\bar{S}_\alpha$, is another (less conservative) alternative for this purpose. The anisotropy index, A_α corresponds to the *coefficient of variance* of the angle-dependent strength S_α. For an SVE with isotropic strength $A_\alpha = 0$. Conversely, it takes higher values as the angular variation of strength increases. In subsequent sections, we use A_α as a measure of fracture strength anisotropy.

2.5 Covariance and Correlation Functions. We are interested in studying how the strength fields change spatially and angularly. The strength field S_α, $\alpha \in \{NH, N, C, S\}$, is a function of space-angle coordinate $\xi = (X, Y; \theta)$. The covariance function between two space-angle coordinates ξ_A and ξ_B for strength S_α is denoted by cov_α and is defined as

$$\begin{aligned}\text{cov}_\alpha(\xi_A, \xi_B) &= \mathbb{E}((S_\alpha(\xi_A) - \mu_A)(S_\alpha(\xi_B) - \mu_B)) \\ &= \mathbb{E}((S_\alpha(\xi_A)S_\alpha(\xi_B))) - \mu_A\mu_B\end{aligned} \tag{12}$$

where $\mathbb{E}$ is the mean value operator and μ_A, μ_B are shorthands for means of S_α at ξ_A and ξ_B; that is, $\mu_A = \mathbb{E}(S_\alpha(\xi_A))$ and $\mu_B = \mathbb{E}(S_\alpha(\xi_B))$.

After the covariance function is calculated, the correlation of the two variables can then be calculated. The Pearson correlation coefficient, referred to as *Pearson's r*, is used to calculate how correlated the two variables are. If r is equal to $+1$, then the two variables are completely positively linearly correlated, while if equal to -1 the variables are completely negatively linearly correlated. An r value equal to 0 means that the two variables are not linearly correlated at all. The correlation function for strength S_α between its values at space-angle coordinates ξ_A and ξ_B is denoted by $\text{corr}_\alpha(\xi_A, \xi_B)$ and is defined by

$$\text{corr}_\alpha(\xi_A, \xi_B) = \frac{\text{cov}_\alpha(\xi_A, \xi_B)}{\varsigma_A \varsigma_B} \tag{13}$$

where ς refers to the standard deviation and ς_A, ς_B are shorthands for the standard deviation of S_α at points ξ_A and ξ_B, respectively. That is, $\varsigma_A = \sqrt{\text{cov}_\alpha(\xi_A, \xi_A)}$ and $\varsigma_B = \sqrt{\text{cov}_\alpha(\xi_B, \xi_B)}$.

These two covariance and correlation functions are then used to determine how fracture strength fields are related in space and in angle. Homogenizing random fields that are consistent with material microstructure, in this context, is of crucial importance for the resulting *stochastic partial differential equations* for elastodynamic fracture problem. Investigating how these fields are related

provide an interesting look at understanding the fracture strength fields for a given material.

2.6 Calculation of Mesoscopic Field Statistics. The statistics of fracture strengths, homogenized at the mesoscale, depend on the statistics of microcracks at the microscale and the size of SVE. As mentioned in Sec. 2.2, two distinct *isotropic* and *anisotropic* microcrack statistics are used at the microscale. We assume that the mesoscopically homogenized fields are *strongly stationary* in space, in that the probability density function (PDF) of $S_\alpha(\xi)$, $\xi = (X, Y; \theta)$, does not depend on its spatial coordinate (X, Y) for all $\alpha \in \{NH, N, C, S\}$; this condition is also referred to as *weakly homogeneous* in homogenization field. This implies that pointwise quantities such as mean $\mathbb{E}(S_\alpha(\xi))$ and variance also only depend on (X, Y). Furthermore, higher-order moments such as covariance function will depend on relative spatial distance of the points, not their absolute spatial position. Thus, in Sec. 3 when the PDFs of S_α are presented, only their angular argument is maintained. Moreover, the spatial dependence of the covariance function in Eq. (12) is only through $\Delta X = X_B - X_A$ and $\Delta Y = Y_B - Y_A$, the spatial difference of ξ_A and ξ_B, and the function can be expressed as

$$\begin{aligned}\widetilde{\text{cov}}_\alpha(\Delta X, \Delta Y; \theta_A, \theta_B) &:= \text{cov}_\alpha(0, 0, \theta_A; \Delta X, \Delta Y, \theta_B) \\ &= \text{cov}_\alpha(X_A, Y_A, \theta_A; X_B, Y_B, \theta_B)\end{aligned} \tag{14}$$

This will be used in reported covariance functions in Sec. 3.3.

The second assumption for the mesoscopic fields is their ergodicity, in that the statistical properties can be deduced from a single, sufficiently large realization of these fields. That is, for either of the two isotropic and anisotropic microcrack models, only one rock domain is realized and subsequently homogenized by the SVEs. This simplifies the computation of PDFs of $S_\alpha(\theta)$ in Secs. 3.1 and 3.2, as the spatial domain PDF of S_α over that single realization is computed and used in lieu of ensemble PDF of $S_\alpha(\theta)$ at a fixed spatial location over many realizations. Moreover, the assumption of the ergodicity for the first moments is used to similarly compute covariance function $\widetilde{\text{cov}}$ in Eq. (14) by moving the base point in one realization, rather than computing the function across many realizations. This assumption is used to compute the covariance (and correlation) functions in Sec. 3.3.

The spatial stationary condition assumption is justified by the fact that the spatial location of microcracks in sample S19 is reported to follow a uniform distribution [33]; as discussed in Sec. 2.2, this would result in a uniform spatial distribution of crack center-points in the pick-and-place algorithm. In addition, if the realized rock domain is large enough, based on the details of domain realization scheme and statistics of microcracks, the statistics of mesoscopic fields homogenized by this realization should be representative of the ensemble statistics; this has been the rationale for assuming ergodicity condition for the pointwise PDF and covariance function. Stationarity and ergodicity assumptions are often used in geo-statics [49] and homogenization [22] fields. It is noted that the weaker wide-sense stationarity, i.e., *second-order stationarity*, is also used in homogenization, e.g., Refs. [20] and [23], where only the mean value and covariance function are stationary. While strong stationarity and the aforementioned ergodicity conditions are used and justified for this study, we emphasize these conditions can be violated in many practical applications; see, for example, the discussion on the stationary condition for geo-masses in Ref. [50].

2.7 Asynchronous Spacetime Discontinuous Galerkin Method. The aSDG finite element method formulated for elastodynamic [41] is used for the analysis of domains with mesoscopic inhomogeneous and anisotropic fracture strength fields. The method utilizes discontinuous basis functions across all element boundaries and directly discretizes spacetime using nonuniform grids that satisfy a special causality constraint; the *Tent Pitcher*

[51] algorithm advances the solution by consequently solving local *patches* (collections) of spacetime elements, until the entire spacetime domain is filled with tetrahedral elements for two-dimensional (2D) problems. Unique properties, such as local and asynchronous solution scheme, arbitrarily high and local temporal order of accuracy, and linear solution scaling versus the number of elements, result in a highly accurate and efficient solution scheme for elastodynamic problem.

An interfacial contact and damage model [52] is used to model the processes of debonding and contact-stick/contact-slip mode transitions in rock. Motivated by a model in Ref. [53], an effective stress scalar value, $\breve{s}$, combines positive normal and shear traction components. The effective stress is used for crack nucleation, propagation direction, and damage evolution criteria; a crack is nucleated at a location $\mathbf{X} = (X, Y)$, if the effective stress at $\mathbf{X}$ exceeds the mesoscopic uniaxial tensile strength field at that location for any angle, that is if $\breve{s}(\mathbf{X}, \theta) \geq S_N(\mathbf{X}, \theta)$ for any $\theta \in [0, 2\pi]$. The crack propagation direction requires extension from a crack tip (or a nucleation point) in a direction θ_{ext} for which $\breve{s}(\theta_{\text{ext}})/S_N(\mathbf{X}, \theta_{\text{ext}})$ is a local maximum and is greater than one. Finally, for a point $\mathbf{X}$ on an existing (or extended) crack surface with angle θ_c, damage evolution is governed by the comparison of the corresponding effective stress and strength; that is $\breve{s}(\mathbf{X}, \theta_c)$ and $S_N(\mathbf{X}, \theta_c)$, respectively. Steps 3 and 4 in Fig. 1 show sample mesoscopic strength fields (at four angles) and a macroscopic fracture response obtained by the aSDG method. We refer the reader to Refs. [14] and [52] for the overview of the damage model and aforementioned fracture criteria.

Three different sets of error indicators and mesh adaptive operations are used to ensure the accuracy of dynamic fracture problem. First, energy dissipation within individual finite elements is used as an error indicator to ensure the accuracy of the solution of elastodynamic problem. Second, an energy-based error indicator is used on contact/fracture surfaces to measure and control the error in satisfying corresponding interfacial constitutive equations [54]. The *h*-adaptive scheme in Ref. [55] simultaneously refines and coarsens the elements in spacetime to ensure the preceding errors are sufficiently small. Third, the fracture propagation criterion based on macroscopic effective stress can predict crack propagation in arbitrary directions. Highly advanced mesh adaptive operations in spacetime modify the spatial front mesh used by the aSDG method to align interelement boundaries with new crack directions [56]. Thus, the method has the flexibility of extended finite element methods (XFEMs) [57,58] and generalized finite element methods (GFEMs) [59,60] without the need to use enriched finite elements. Moreover, for rock fracture, particularly in dynamic regime and in the presence of material inhomogeneities, highly complex features such as microcracking, crack branching, and crack intersection are observed that cannot be easily modeled with XFEMs and GFEMs. We refer the reader to Ref. [61] for a more thorough discussion on the advantages of the aSDG method to XFEMs and GFEMs.

3 Numerical Results

The numerical results for each domain, isotropic and anisotropic, will be presented here. Each domain is rectangular, centered at $\mathbf{X}_{\text{center}} = (0, 0)$ and spans 40 mm in both X and Y directions, i.e., the domain spans from $[-20, -20]$ to $[20]$. As described in Sec. 2.2, the microcrack statistics of S19 Yuen-Long marble sample from Ref. [33] is used to create the two domains. For the half-crack length power law distribution, the power law Cauchy distribution exponent z is equal to 2.017 and the distribution numerator $q*V_0$ is equal to 0.007. A mean crack length is $2a = 0.141$ mm. The minimum half crack length of a' is defined as 0.0075 mm, or $2a' = 0.015$ mm. This minimum crack length is used to define S_{max}. The crack density is $\varepsilon_0 = 0.243$.

The isotropic domain has a uniform crack angle distribution between [0, 360] deg and has no angular bias. Crack angle for the anisotropic domain has a triangular distribution with the range of [25,35] deg and a peak value of 30 deg. The material Poisson's ratio is 0.25, and Young's modulus is 34.65 GPa. The result of the SVE analysis is shown below for each domain. The generated microcrack domain is shown in Fig. 4, and the given length and angle PDFs are shown in Fig. 5.

3.1 Isotropic Domain. As detailed previously, the isotropic domain has a uniform crack distribution of θ_c in [0, 360] deg. The SVE analysis process was used to process the microcrack domain to develop mesoscopic strength fields using multiple SVE sizes: $L_{\text{SVE}} = 1, 2, 4$, and 8 mm. Since fracture strengths are assigned at the centers of the SVEs, the edge size of the square region for which fracture strength is assigned is $40 - L_{\text{SVE}}$ mm, with the smallest value of 32 mm for $L_{\text{SVE}} = 8$ mm. This explains why larger 40×40 mm^2 domains are considered in Fig. 4, so that the smallest edge size of the mesoscopic fracture strength fields matches the 32 mm edge size of the VEs in Ref. [33]. From here on, all homogenized mesoscopic strength fields are shown in a square with 32 mm edge size.

The loading angle θ was varied between [0, 180] deg with a discrete angular spacing of 2 deg within this range, resulting in 90 discrete loading angle strength fields. The minimum uniaxial tensile, uniaxial compressive, shear, and hydrostatic tensile fracture strengths were calculated for every crack in the domain, with the minimum strength retained for each SVE.

At a glance at Fig. 6, there is no discernible trend showing a change of strength depending on the loading angle for an isotropic domain. By calculating the statistics of the mesoscopic strength field, the PDF of the strength field at each discrete loading angle can be compared. From Fig. 7, the PDF for each loading angle confirms that general strength of the domain does not change depending on the loading angle, as there is no bias in the direction of microcracks.

The effect of SVE size on homogenized strengths is shown in Fig. 8. As the SVE size increases, the (spatial) variation of homogenized S_N and its corresponding mean value decrease. This is the well-known *size effect* for quasi-brittle materials [3,5]. As L_{SVE} increases, the SVE tends to the RVE limit, explaining the decrease in the variation of homogenized strengths. Also, the likelihood of containing larger cracks increases as L_{SVE} increases. This explains the decrease in the overall values of S_N. Again, the PDF of the strength field shown in Fig. 9 agrees with this analysis. As the SVE size increases, the mean strength of the field decreases and the standard deviation of the response becomes smaller. It is noted that if L_{SVE} were chosen sufficiently smaller than 1 mm, many SVEs would contain no cracks and would be assigned the strength S_{max}, as described in Sec. 2.3. This would result in a bimodal PDF for S_N; see, for example, Fig. 9 in Ref. [32].

We use A_N to study the anisotropy of the homogenized strength field S_N. A field of anisotropy index is constructed by assigning the value of A_N for each SVE at its centroid. While the measure of anisotropy is defined for all angle-dependent strengths in Eq. (11c), the results are only presented for S_N.

Figure 10 shows the spatial distribution of A_N for different SVE sizes. While for easier comparison of results, the maximum limit of 1 is used in all contour plots, A_N can be arbitrarily high. Since the distribution of crack angle is uniform in [0, 360] deg, we expect the macroscopic response of the domain to be isotropic. That is, A_N should tend to zero at all points as L_{SVE} increases toward infinity. This aspect can be observed in the figure. For the smallest SVE size in Fig. 10(a), A_N varies with almost the same high spatial frequency that S_N fields varies in Fig. 6. There are several islands of high anisotropy measures that are caused by highly anisotropic distribution of microcrack angles in these regions. Some of the zones with the highest values of A_N are framed in the figure. For larger SVE sizes in Figs. 10(b)–10(d), the intensity of the anisotropy index at the peak points decreases and the field is generally smoothed. The same argument that is
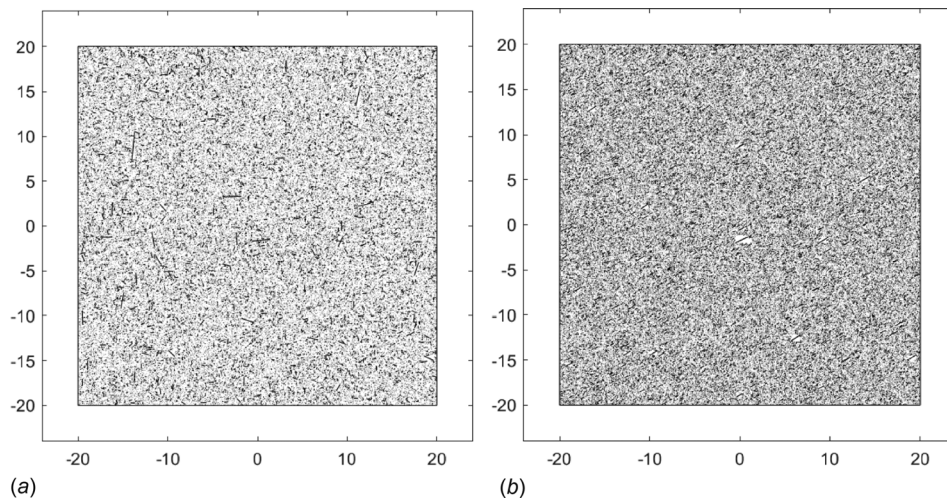
Fig. 4 Generated microcrack domains: (a) isotropic domain and (b) anisotropic domain

used in the decrease in fracture strength in Figs. 8 and 9 for larger SVE sizes applies here; for this macroscopically isotropic material, the angle distribution of the most critical (longest) cracks within an SVE tends to its macroscopic uniform distribution of [0, 360] deg. The spatial variation of this field also decreases, again, because the SVEs tend to the RVE limit. However, for $L_{\text{SVE}} = 8$ mm, the same islands of high A_N persist, even though

Fig. 5 Generated microcrack domain crack PDFs: (a) length 2a (mm) and (b) θ_c (deg)

their intensity and sharpness have significantly decreased compared to those in Fig. 10(a).

3.2 Anisotropic Domain. The anisotropic domain was generated with a triangular distribution in crack angle, with a peak of $\theta_c = 30$ deg and a range of [25,35] deg; cf. Fig. 5(b). Therefore, the lowest fracture strengths should be for loading angles close to $\theta = 30$ deg, since this loading angle will effectively be pulling the cracks open. The maximum strength of SVEs should be close to $\theta = 120$ deg, since this is pulling the cracks almost parallel to their direction.

By viewing Fig. 11, the differing trend in strength based on loading angle can be seen. Loading angles of $\theta = 120$ deg creates a uniform, homogeneous high strength field equal to S_{max}, corresponding to minimum crack length $2a' = 0.015$ mm; since most cracks are almost parallel to loading angle, i.e., $\theta_d \approx \pi/2$, $s_N(\theta)$ tends to infinity in Eq. (9b). At 90 deg apart from this, $\theta = 30$ deg, a nearly uniform low-strength field is observed in Fig. 11(a). This trend is confirmed by the PDF of the strength field by varying the loading angle, as shown in Fig. 12. As the strength gets closer to the θ of minimum strength for the anisotropic domain, the mean strength steadily decreases. When comparing the isotropic PDF shown in Fig. 7 to the anisotropic PDF shown in Fig. 12, the effect of anisotropic crack distributions can be shown clearly. An interesting note to this is that for anisotropic domains, the actual strength of the field can be much higher over a wide range of loading angles compared to isotropic domains. Understanding the anisotropy of a given material can be crucial to whether a given material could be used for a specific application and loading condition.

Figure 13 shows the spatial distribution of the anisotropy measure for the anisotropic domain for different SVE sizes. Since microcrack angles are biased around $\theta_c = 30$ deg, this domain is anisotropic even when the VE size tends to infinity; the lowest and highest strengths are expected at angles $\theta_d = 30$ and $\theta_d = 120$ deg, respectively. Overall, as the SVE size increases, the spatial frequency of variations of A_N decreases and the field becomes more uniform. This is because the SVE tends to the RVE size limit.

Another observation is that the averaged fracture strength field S_N is less anisotropic for smaller SVE sizes. As the L_{SVE} increases, there are more microcracks contained in an SVE and very low strengths are expected for θ_d in [25,35] deg, particularly for the mode of the crack angle distribution $\theta_d = 30$ deg. This results in a highly angle-dependent, yet more spatially uniform distribution for S_N, reflected in more uniform and higher values for A_N in Figs. 13(c)–13(d). In contrast, for smaller SVEs, there is
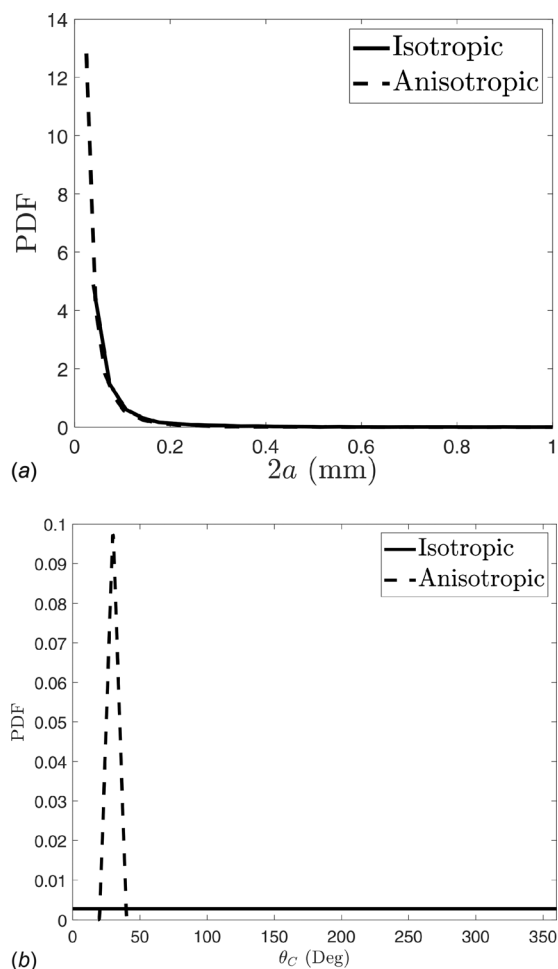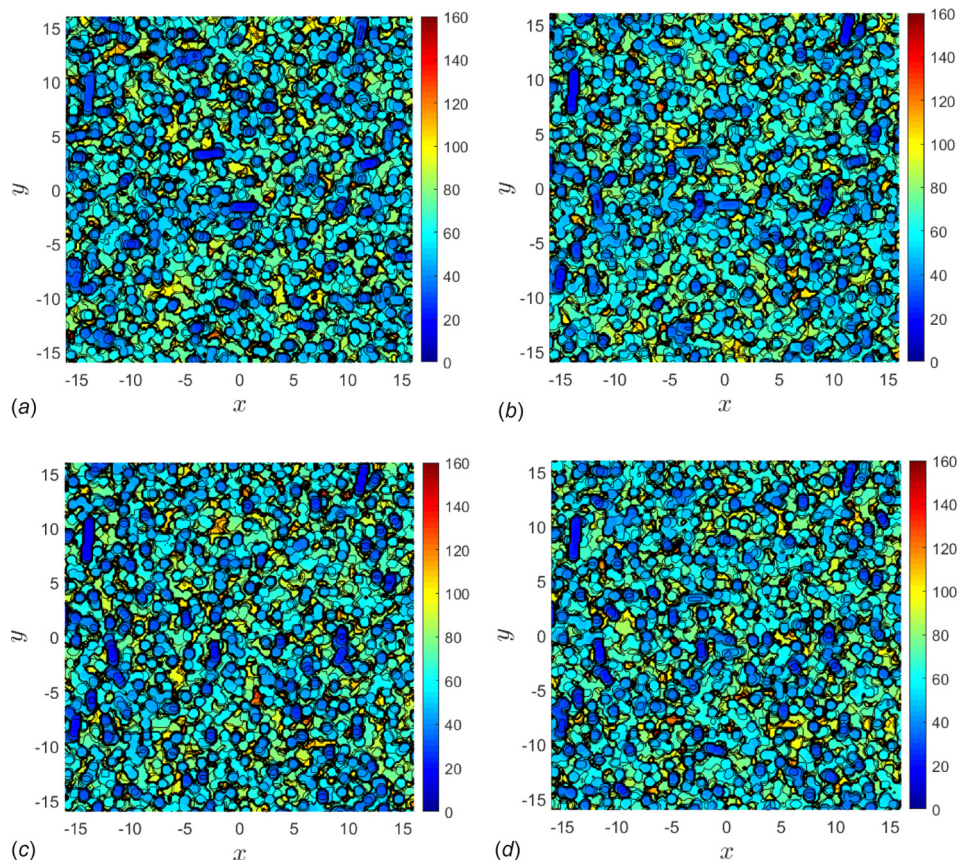
Fig. 6 $S_N(\theta)$ mesoscopic isotropic strength fields ($L_{\mathrm{SVE}} = 1$ mm) at various θ: (*a*) $\theta = 30$ deg, (*b*) $\theta = 60$ deg, (*c*) $\theta = 90$ deg, and (*d*) $\theta = 120$ deg

a higher variability in angles within [25,35] deg that have the longest cracks, thus the lowest strengths, within the SVEs. Thus, the averaged strength field is less anisotropic, yet more spatially variable due to higher variability of the statistics of microcracks within the SVEs. The frames regions in Fig. 13 demonstrate that, similar to Fig. 10, the regions of higher anisotropy are preserved and averaged as the SVE size increases.

To represent this difference in the isotropic and anisotropic domains, four SVEs were selected based on the measure of anisotropy, A_N. Four points, chosen from the lowest measure of anisotropy to highest in the isotropic domain, are shown in Figs. 10(*a*)
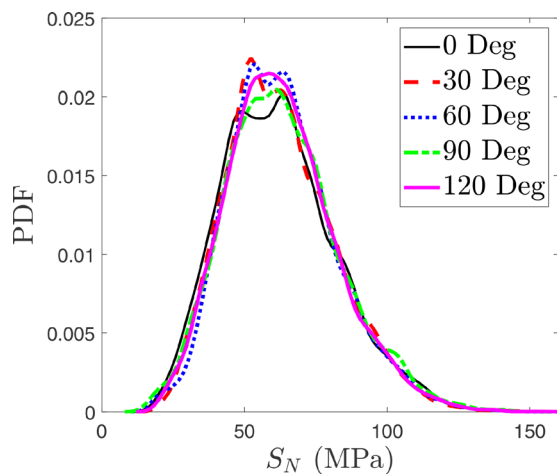
Fig. 7 Isotropic $S_N(\theta)$ PDF for varying θ

and 13(*a*). While the two domains do not have the same microcrack distribution and are unrelated, the same points were used for both isotropic and anisotropic domain. P2 in the isotropic domain was selected such that it corresponded to the same coordinates as the location of the highest anisotropy in the anisotropic domain. The coordinates of each point, measure of anisotropy A_N, and mean strength $\bar{S}_N$ are shown in Table 1, and how the respective uniaxial strength field $S_N(\theta)$ changes in angle is shown in Fig. 14.

For the isotropic domain, as A_N increases, the strength field becomes more anisotropic, dominated by one angle of the highest and lowest strength. The standard deviation increases such that the peak and minimum strength are further away from the given mean strength. For the isotropic domain, each SVE contains a different angle of maximum and minimum strength. The measure of anisotropy is a good indicator for the relative dominance of one crack angle contained in that SVE.

The anisotropic domain contains a dominant angle of maximum strength no matter the level of anisotropy. In the anisotropic domain, $P2$ contains the highest measure of anisotropy. As is expected, the width of the angular band of maximum strength for $P2$ is also the narrowest, as shown in Fig. 14(*b*). Generally, while the angle of maximum and minimum strength is roughly the same for all SVEs in the anisotropic domain, the measure of anisotropy indicates how narrow the band of maximum and minimum strength is, which is caused by the SVE only containing cracks within a narrow angular distribution.

In short, for the isotropic domain, measure of anisotropy is higher for smaller SVEs and it tends to zero for larger SVEs, as shown in Fig. 10. In contrast, for the anisotropic domain, A_N tends to a finite high value for larger SVEs and it takes lower values for smaller SVEs. For both cases, the homogenized strength fields are more inhomogeneous for smaller SVE sizes. Since maintaining
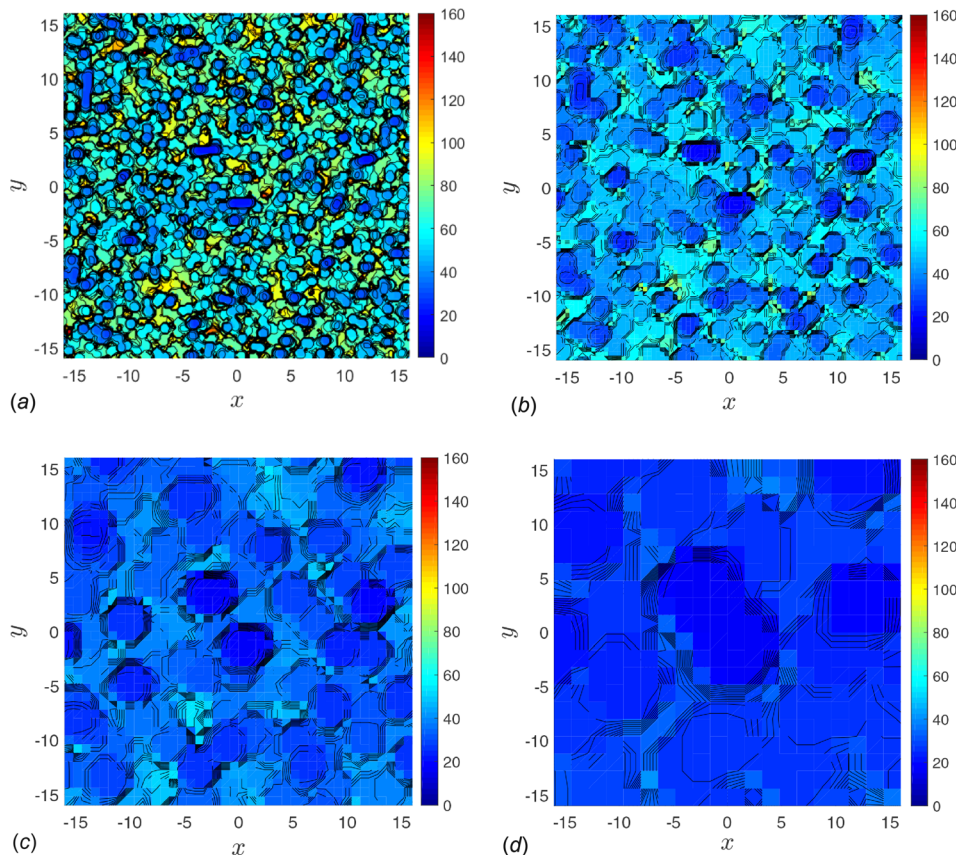
Fig. 8 $S_N(\theta)$ **mesoscopic isotropic strength fields** ($\theta = 0\,$deg) **for different SVE sizes:** (a) $L_{\text{SVE}} = 1\,$mm, (b) $L_{\text{SVE}} = 2\,$mm, (c) $L_{\text{SVE}} = 4\,$mm, and (d) $L_{\text{SVE}} = 8\,$mm
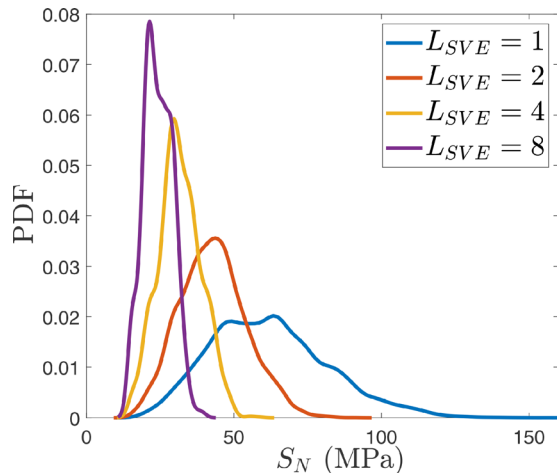
Fig. 9 Isotropic S_N PDF for varying SVE size L_{SVE}

material inhomogeneity is desirable in fracture analysis, the smaller SVE size $L_{\text{SVE}} = 1\,$mm is used to produce mesoscopic strength fields for the macroscopic simulations in Sec. 3.4.

3.3 Covariance and Correlation. We first study the dependence of the covariance and correlation functions on space and angle coordinates for S_N. Next, the correlation between different angle-independent strengths derived from S_α, $\alpha \in \{NH, N, C, S\}$ is investigated. In the following, we use the assumed stationarity and ergodicity discussed in Sec. 2.6 to compute the covariance and correlation functions based on only the single realization for

each rock model, and to express the covariance function as a function of spatial distance of the two points; cf. Eq. (14).

3.3.1 Spatial Correlation. We first analyze the form of covariance function in space. That is, ξ_A and ξ_B are chosen such that the same loading angle is chosen for both, meaning that $\theta_A = \theta_B$. For this analysis, we use the strength field S_N homogenized by $L_{\text{SVE}} = 1$. Moreover, $\theta_A = \theta_B$ is set to zero to focus on spatial correlation of uniaxial tensile strength for zero degree loading direction. This *spatial covariance function* of S_N for zero loading direction is only a function of change of spatial coordinate $(\Delta X, \Delta Y)$ and is denoted and defined by $\text{cov}_{\mathbf{X}N}(\Delta X, \Delta Y) = \overline{\text{cov}}_N(\Delta X, \Delta Y; 0, 0)$. This function can be evaluated from a single homogenized strength field by moving the space position of ξ_A and keeping the spatial difference of ξ_B and ξ_A fixed and equal to $(\Delta X, \Delta Y)$.

Figure 15 shows $\text{cov}_{\mathbf{X}N}$ for both isotropic and anisotropic microcrack statistics. Several observations can be made. First, from the circular contour lines, it is evident that the covariance function is only a function of the relative distance of the two points and not their relative angle. That is the spatial covariance beyond being homogeneous (depending on only on relative spatial difference of ξ_A and ξ_B) is also isotropic (not being a function of relative spatial angle between ξ_A and ξ_B). Second, we observe that the spatial covariance function quickly tends to zero in a spatial range roughly equal to the SVE size. This corresponding to traversing about 5 SVEs as n is chosen equal to 5; cf. Sec. 2.1. Third, the spatial covariance function has an almost identical form for both isotropic and anisotropic microcrack distribution models.

3.3.2 Angular Correlation. Next, we analyze the form of the covariance function in angle. That is, ξ_A and ξ_B share the same spatial location (X, Y), but have arbitrary angles $0 \le \theta_A$, $\theta_B < \pi$. Again, considering S_N for $L_{\text{SVE}} = 1$, this covariance function is
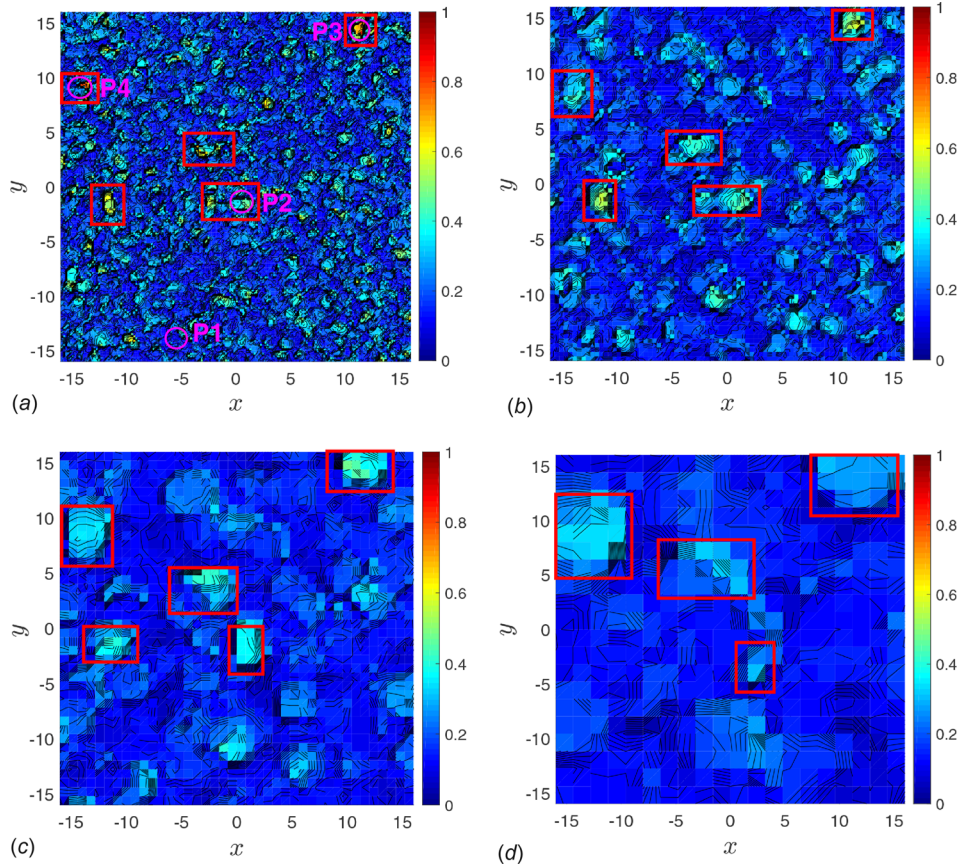
Fig. 10 Measure of anisotropy, A_N, for the macroscopically isotropic domain for different SVE sizes: (a) $L_{SVE} = 1$ mm, (b) $L_{SVE} = 2$ mm, (c) $L_{SVE} = 4$ mm, and (d) $L_{SVE} = 8$ mm

defined and denoted by $\text{cov}_{\theta N}(\theta_A, \theta_B) = \overline{\text{cov}}_N(0, 0; \theta_A, \theta_B)$. Similar to the calculation of $\text{cov}_{\mathbf{X}N}$, the spatial stationarity of homogenized strength fields is used to populate the statistics for $\text{cov}_{\theta N}$ by moving (X, Y) in a realization of S_N.

Several observations are made for $\text{cov}_{\theta N}$ of the isotropic domain in Fig. 16(a). First, the value of the function along the diagonal line $\theta_A = \theta_B = \theta$ corresponds to $\text{cov}_{\theta N}(\theta, \theta)$, the variance of the uniaxial tensile strength for angle θ. Since the orientation of microcracks is isotropic (uniform in $[0, \pi]$), we expect the statistics of $S_N(X, Y, \theta)$ to be stationary in θ as well, that is, independent of the angle of loading. Consequently, the variance of $S_N(\theta)$ too should be independent of θ, meaning that the value of $\text{cov}_{\theta N}(\theta_A, \theta_B)$ on diagonal $\theta_A = \theta_B = \theta$ should be constant. The small variations of $\text{cov}_{\theta N}$ on this diagonal in Fig. 16(a) are contributed to numerical errors associated with the finite set of values used in evaluating the covariance function.

Second, again from the stationary condition of S_N in θ, $\text{cov}_{\theta N}(\theta_A, \theta_B)$ should only be a function of the relative difference of the angles $\theta_B - \theta_A$ rather than their individual values. Since $S_N(X, Y, \theta)$ is periodic in θ with period π, $\text{cov}_{\theta N}(\theta_A, \theta_B)$ is a periodic function with the solution in $[0, \pi) \times [0, \pi)$ (the part shown in the figure) repeating in 2D $(\theta_A, \theta_B) \in \mathbb{R}^2$ angle space. Considering these facts, the value of the function only depends on the distance of the point (θ_A, θ_B) from the diagonal $\theta_A = \theta_B$ line. Again, the small deviation of the $\text{cov}_{\theta N}$ from this condition in Fig. 16(a) is a consequence of the finite number of points used for computing the covariance function. Finally, we observe that the covariance function tends to zero for an angle difference of about $|\theta_B - \theta_A| = 30$ deg.

The covariance function in angle for the anisotropic domain is shown in Fig. 16(b). Again, the value on the diagonal $\theta_A = \theta_B = \theta$ is the variance of $S_N(\theta)$. For the anisotropic domain, the highest variances of $S_N(\theta)$ are observed at angles about 10 deg outside the

angles corresponding to the highest strength around 120 deg. The observed high variance is a consequence of stipulating a maximum strength corresponding to minimum allowable crack length $2a'$; cf. Sec. 2.2. Overall, we observe a much more complex form for the covariance function of anisotropic domain compared to that in Fig. 16(a); specifically, due to the anisotropy of $S_N(\theta)$, $\text{cov}_{\theta N}(\theta_A, \theta_B)$ is no longer only a function of the angle difference $|\theta_A - \theta_B|$.

The angular correlation function, defined by $\text{corr}_{\theta N}(\theta_A, \theta_B) = \text{corr}_N(X_A = X, Y_A = Y, \theta_A; X_B = X, Y_B = Y, \theta_B)$, is shown for isotropic and anisotropic rock domains in Fig. 17. As expected, strengths $S_N(X, Y, \theta_A)$ and $S_N(X, Y, \theta_B)$ are highly correlated as the angle difference tends to zero. In fact, for $\theta_A = \theta_B = \theta$, by definition the correlation is one, given that the two strengths coincide. This corresponds to the value of one on diagonal line $\theta_A = \theta_B$ for both cases in Fig. 17. For isotropic rock, fracture strengths are highly correlated for an angle difference $|\theta_B - \theta_A|$ roughly less than 30 deg, and the correlation is almost zero for higher angle differences. The zero correlation of fracture strength for this high of an angle difference can be compared to zero correlation between the strength of two points that are roughly 1 mm apart in Fig. 15.

The angular correlation of S_N for the anisotropic domain is vastly different; aside for a 10 deg range centered around 120 deg, the angle corresponding to the highest strengths, fracture strength of any two angle of loading are highly correlated. This is due to the fact that the majority of cracks are aligned close to 30 deg, and in approximate sense, $1/\cos(\theta - 30)$ is the factor that relates strength at angle θ to that for the 30 deg, i.e., the weakest strength; cf. Eq. (9b) and note that $\theta_d \approx \theta - 30$. Clearly due to the local variation of crack angle in the range [25,35] deg, there is not this perfect correlation between S_N at two arbitrary angles; however, correlations close to one are observed in Fig. 17(b). The zero
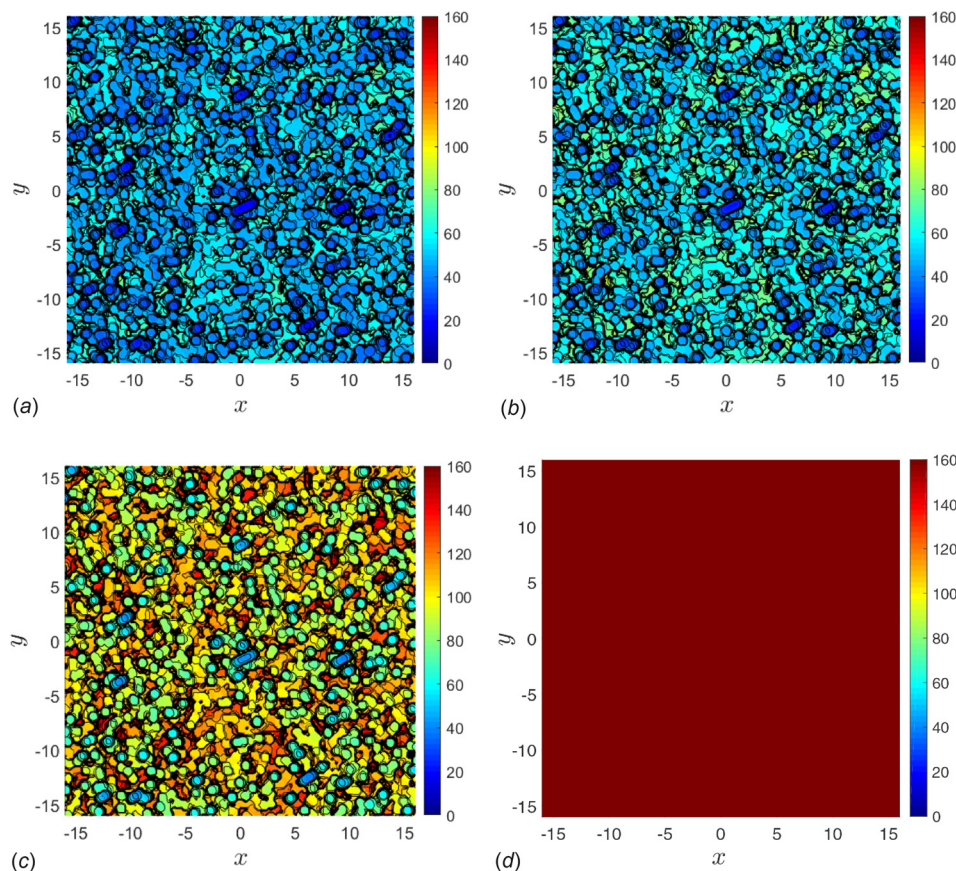
Fig. 11 S_N mesoscopic anisotropic strength fields ($L_{SVE} = 1$ mm) at various loading angles: (a) $\theta = 30$ deg, (b) $\theta = 60$ deg, (c) $\theta = 90$ deg, and (d) $\theta = 120$ deg

correlation of high strength angle range and other angles is contributed to assigning S_{max} for angles around 120 deg.

3.3.3 Correlation Between Different Strength Types. Finally, we study the correlation between different fracture strength fields. To more effectively focus on the type of strength, rather that angle-dependent strengths $S_\alpha(\theta)$, we use the two alternatives of SVE angle-independent strengths proposed in Sec. 11. The $\bar{S}_N$, $\bar{S}_S$, and $\bar{S}_C$ in Eq. (11a) provide an overall average angle-independent strength for an SVE. In contrast, $m(S_N)$, $m(S_S)$, and $m(S_C)$ are the most conservative choices by taking the minimum of strengths over all angles of loading in Eq. (11b). When for a given L_{SVE}, i.e., observation size, strength anisotropy is low, either of these two choices of strength can be used to define a unique isotropic strength for a given spatial location. For example, we have used the mean and min of uniaxial normal strengths for two different types of composites in Refs. [62] and [63], respectively. However, in these works only macroscopically isotropic materials were considered and the correlation between different strength types was not studied.

The Pearson correlation coefficient between these six derived angle-independent and inhomogeneous strength fields and the already angle-independent strength S_{NH} are provided in Table 2 for the isotropic domain. Very high correlations are observed between S_N, $\bar{S}_N$, $\bar{S}_S$, and $\bar{S}_C$. The lowest value corresponds to a correlation of 0.847 between S_{NH} and $\bar{S}_C$. This can be contributed to pure mode *I* and mode *II* fracture for hydraulic tensile and uni-axial compressive loadings, respectively. In addition, for a single crack s_C is highly anisotropic, and even in the zone for which s_C is finite, its value quickly tends to infinity; cf. Eq. (9c) and Fig. 3. The highly different fracture modes for a single crack explains the lower correlation between S_{NH} and $\bar{S}_C$, even after the operations

(10) and (11b) are taken into account to derive these angle-independent SVE strengths.

However, if instead of using angular mean of strengths in an SVE, their minimum value is used, and a perfect correlation is observed between S_N, $m(S_N)$, $m(S_S)$, and $m(S_C)$. By inspecting Fig. 3 and Eq. (9), we observe that the angular minimum of all strengths s_N, s_N, s_S, and s_C is the same. Thus, from Eqs. (10) and (11a), for all $\alpha \in \{NH, N, C, S\}$, $m(S_\alpha) = K_c / \sqrt{\pi a_{max}}$, where a_{max} is the maximum half-length of a crack within an SVE. That is, S_N, $m(S_N)$, $m(S_S)$, and $m(S_C)$ are all equal, explaining their perfect correlation.
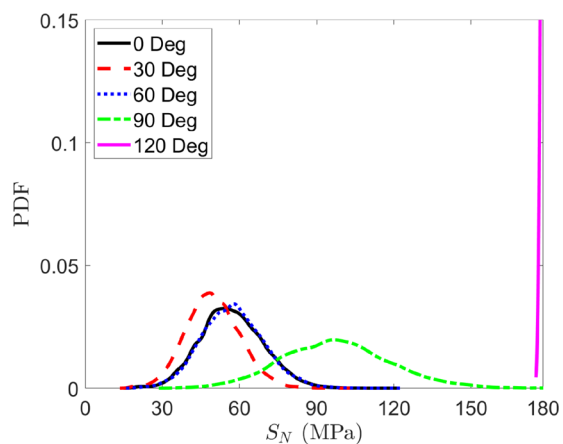
Fig. 12 Anisotropic S_N PDF for varying θ
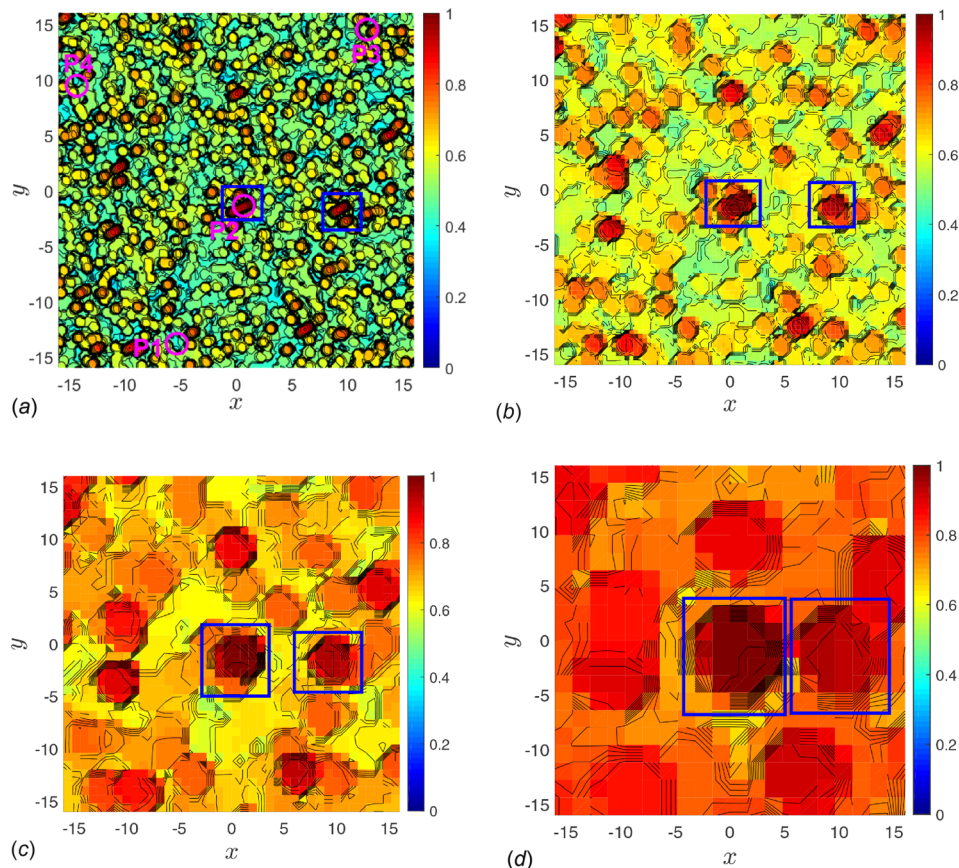
Fig. 13 The measure of anisotropy, A_N, for the anisotropic domain for different SVE sizes: (a) $L_{SVE} = 1$ mm, (b) $L_{SVE} = 2$ mm, (c) $L_{SVE} = 4$ mm, and (d) $L_{SVE} = 8$ mm

From the preceding comparison of $\bar{S}_\alpha$ and $m(S_\alpha)$, it appears that if one aims to simplify the fracture strength fields by eliminating their angular-dependency, the mean value is a more appropriate choice for microcracked domains as it maintains the fundamental differences between different types of strength. Also, as elaborated in Ref. [62], the use of angular minimum strengths can be too conservative.

The correlation coefficients for the anisotropic domain are provided in Table 3. As explained, the correlation between all minimum strengths and S_{NH} is one. For the mean strengths, the correlations are considerably higher than those for the isotropic domain, with a minimum value of 0.967. Similar to high correlation of strength between different angles of loading in Fig. 17, this can be contributed to large percentage of cracks being oriented close to 30 deg and more or less constant factors between different fracture types in Eq. (9) for $\theta_c \approx 30$ deg.

From the comparison of the results for isotropic and anisotropic domains, it is suggested that eliminating fracture strengths S_S and S_C in a failure criterion and maintaining only S_N is a more sensible choice for anisotropic domains. Under such conditions, the other strengths can be approximated as constant factors of uniaxial tensile strength field, without introducing much error. This greatly simplifies several aspects of the proposed multiscale approach in this manuscript, as we consider a single inhomogeneous strength field for S_N in Sec. 3.4.

In this section, we studied how fracture strengths vary by changing the spatial location, angle of loading, and type of strength. Covariance functions can be used by the Karhunen–Loéve [64,65] or other similar methods to generate a large number of random field realizations that are consistent with fields homogenized with a given L_{SVE}. This approach in general is faster than generating domains with an actual microstructure (i.e., the microcracks here) and using the SVEs to homogenize them. Thus, understanding the form of covariance function is of great importance. For the two microcrack distributions considered and for $L_{SVE} = 1$, the corresponding random fields are stationary in space. In addition, the spatial covariance function is spherical and tends to zero at a length scale below L_{SVE}. The angular covariance function is stationary in angle for the isotropic domain and tends to zero for loading angle differences greater than about 20 deg.

3.4 Dynamic Fracture Analysis. For fragmentation and other problems that lack macroscopic stress concentration points, maintaining material inhomogeneity is of great importance. We study the fragmentation of a 32×32 mm^2 square rock domain (same VE size used in Ref. [33]) under bi-axial tensile loading condition. We use the inhomogeneous fracture strength fields for $L_{SVE} = 1$ for both isotropic and anisotropic domains, to maintain the highest level of material inhomogeneity with the SVE sizes considered. Since $n = 5$, cf. Sec. 2.1, any of the fracture strength fields for $S_N(\theta)$ is represented by a 160×160 resolution *material property* mesh. The value at each grid point is equal to $S_N(\theta)$ obtained for the SVE centered at that point. Using a step size of 2 deg for θ, 90 strength fields $S_N(\theta)$ are computed and stored for macroscopic fracture analysis for each of the two rock domains.

Table 1 Selected SVE location, measures of anisotropy A_N, and mean strengths $\bar{s}_N$

| Points	X	Y	$A_{N,iso}$	$A_{N,aniso}$	$\bar{S}_{N,iso}$	$\bar{S}_{N,aniso}$
P1	−5.4	−13.8	0.093	0.401	81.1	114.4
P2	0.6	−1.4	0.457	0.964	37.5	93.5
P3	11.6	14.4	0.701	0.539	54.6	109.2
P4	−14.2	9.4	0.800	0.406	65.7	96.0

Four of such meshes for isotropic and anisotropic domains are shown in Figs. 6 and 11, respectively.

Initial and boundary conditions were applied consistent with a uniform, isotropic tensile field that ramps linearly in time. The components of the displacement field (U, V) are

$$U(X, Y, t) = \dot{\varepsilon} X t, \quad V(X, Y, t) = \dot{\varepsilon} Y t \quad (15)$$

where (X, Y) and t are space and time coordinates, and $\dot{\varepsilon}$ is the specified normal strain rates for both X and Y directions. Dirichlet boundary conditions, i.e., a prescribed velocity field, is applied on the entire boundary of the domain at all times. This resembles a *displacement control* loading in dynamics and is more appropriate than Neumann boundary condition for capturing the unloading part of macroscopic strain versus stress response. Plane strain conditions were specified with material properties taken from Ref. [33]; that is, Young's Modulus $E = 65$ GPa, mass density $\rho = 2700$ kg/m^3, and Poisson's ratio $\nu = 0.3$. The macroscopic fracture simulations are performed by the aSDG method, described in Sec. 2.7.

Both rock domains are simulated up to time $t = 12\ \mu s$. A strain rate of $\dot{\varepsilon} = 20/s$ is used to gradually load them. A spatially uniform and temporally increasing stress response persists until the stress value reaches the minimum tensile strength of $S_N(X, Y, \theta)$ over all spatial points and angles of loading, at location (X_m, Y_m) and for the angle of loading θ_m. At this instant, a crack is nucleated at (X_m, Y_m) and propagated along the direction θ_m. The uniform stress field no longer persists past this instant, and more cracks are nucleated and/or propagated until the square domain completely fails.
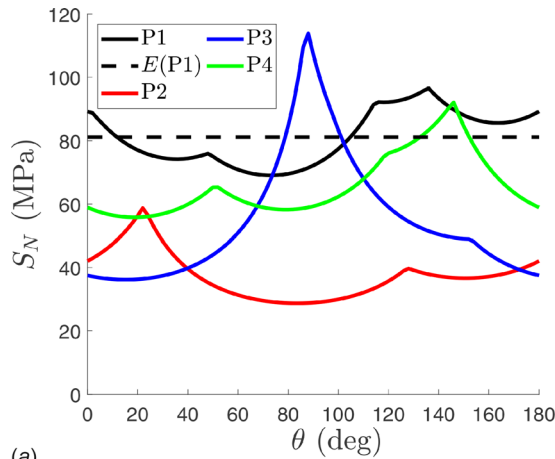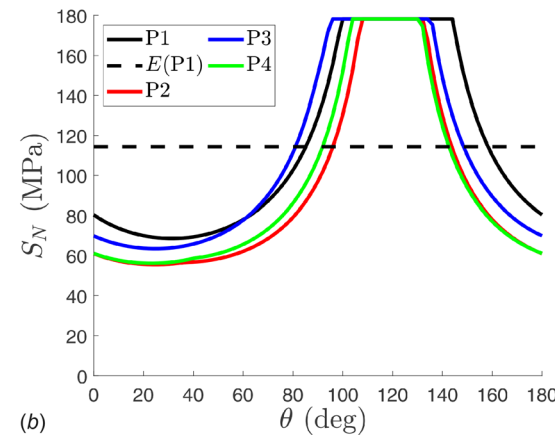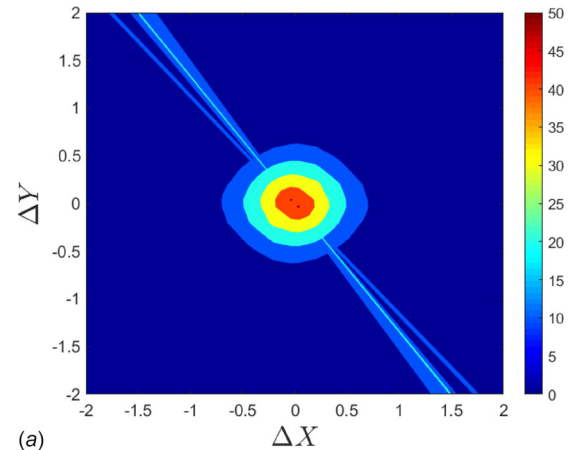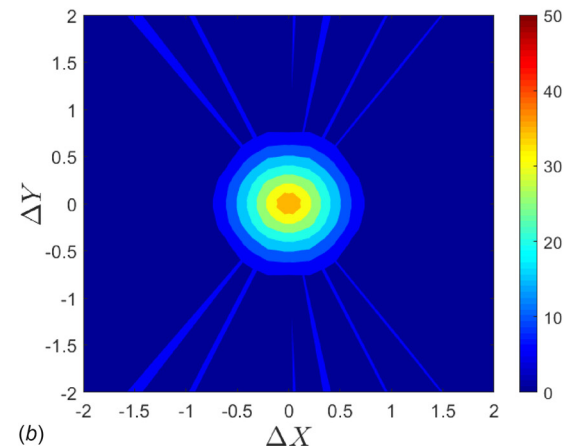
We use homogenization boundary integrals [66] to obtain macroscopic strain E and stress Σ tensors for each time $t \in [0, 12\ \mu s]$. Figure 18 compares the response of the two rock domains in terms of their macroscopic strain versus stress response. The maximum attainable stresses of the isotropic domain are max $(\Sigma_{XX}) = 19.16$ MPa and max $(\Sigma_{YY}) = 18.39$ MPa. The corresponding values for the anisotropic rock domain are max $(\Sigma_{XX}) = 21.82$ MPa and max $(\Sigma_{YY}) = 21.94$ MPa. Thus, the anisotropic rock domain has a higher macroscopic strength under the bi-axial tensile loading condition. This is due to the fact that over the majority of angles, the fracture strength S_N is much higher than the isotropic domain other than a small angular range about the angle of weakest strength. At time $t = 12\ \mu s$, the isotropic domain has reached failure, but the anisotropic domain has not yet reached failure.

Another interesting feature is that for the anisotropic rock, aside from a small region early in macroscopic failure initiation stages, Σ_{YY} is lower than Σ_{XX} over a zone where significant macroscopic softening and unloading occurs in Fig. 18(b). Eventually, however, both stresses take almost the same values once they tend to zero past this zone. Given that for the anisotropic domain, the lowest strengths in the homogenized $S_N(X, Y, \theta)$ field are for angles $\theta \in (25, 35)$ deg; overall, the domain is expected to have a lower strength in Y, compared to X, direction. For the single realization of the microcracks with anisotropic angle statistics in Fig. 4(b), this happens for the range of strains discussed previously. We have repeated the fracture analysis of the same two rock domains under different loading rates $\dot{\varepsilon}$. While the results are not presented for brevity, the same difference between Σ_{XX} and Σ_{YY} for the anisotropic domain is observed for other loading rates. In addition, maximum macroscopic stresses of the anisotropic
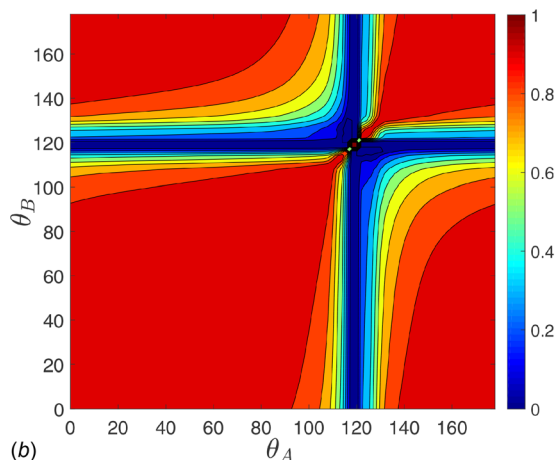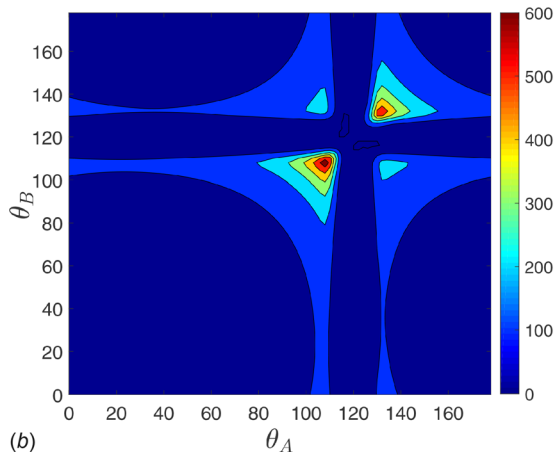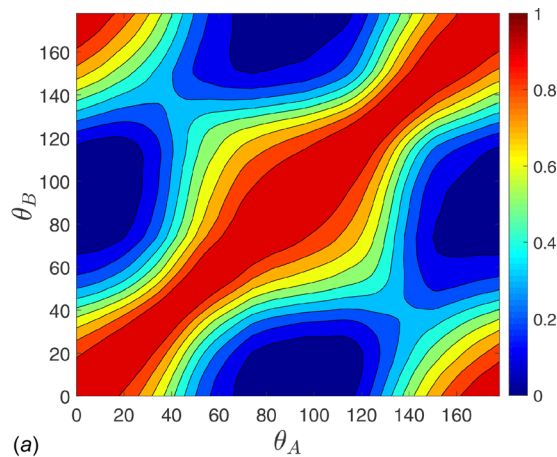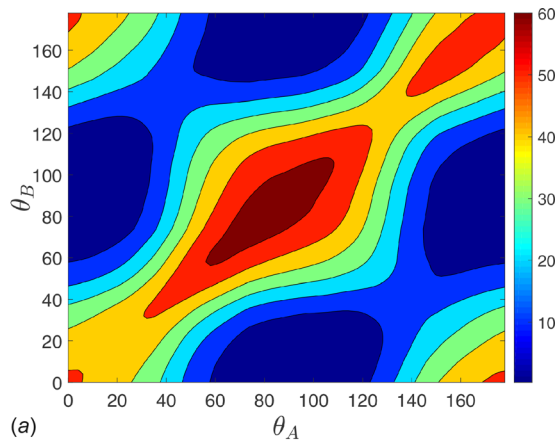

(a)

(b)

Fig. 14 $S_N(\theta)$ for four $L_{SVE} = 1$ mm SVEs with different measures of anisotropy A_N, $\theta = [0, 180]$ deg: (a) isotropic domain and (b) anisotropic domain

(a)

(b)

Fig. 15 Spatial covariance function for strength field S_N, cov$_{XN}$: (a) isotropic domain and (b) anisotropic domain

Fig. 16 Angular covariance function for strength field S_N, $cov_{\theta N}$: (a) isotropic domain and (b) anisotropic domain

Fig. 17 Angular correlation function for strength field S_N: (a) isotropic domain and (b) anisotropic domain

domain consistency remain higher than those of the isotropic domain.

The strain and kinetic energy densities of the two solutions are shown in Fig. 19 for $t = 12$ μs. The strain energy density is mapped to the color field, where light to dark color indicates a range of zero to 1000 J/m³. The kinetic energy is mapped to the height field such that regions of high kinetic energy appear closer. Because the anisotropic domain has not reached failure, higher strain levels are shown in the domain. The isotropic domain shows cracks growing in several directions; however, the anisotropic domain shows the angularly biased crack field where, as expected, the majority of cracks are aligned close to 25–35 deg. The majority of cracks with other orientations connect three to four main cracks that are aligned with the weakest plane of the rock.

Figure 20 depicts the front meshes at the time of failure $t = 12$ μs for the two rock domains. These meshes show the adaptivity of the aSDG method for propagating cracks and controlling solution errors. In addition, the level of interfacial damage parameter is indicated by blue (zero damage) to red (full damage) colors on crack surfaces. For both cases, the solution starts with a spatial triangulation containing no cracks. The effect of initial microcracks in the domain is modeled by anisotropic and inhomogeneous mesoscopic fields of S_N as those shown in Figs. 6 and 11. As the cracks are nucleated with specified propagation directions, the front mesh is continuously adapted to align element boundaries with the specified directions. In addition, adaptive operations ensure that the numerical errors in the bulk and on fracture surfaces are below the user-specified tolerances. This is reflected in finer elements closer to the crack tips in the figure. As a result of these adaptive operations, the front meshes in Figs. 20(a) and 20(b) contain 23,891 and 26,615 triangles, respectively, compared to only 803 triangles in the initial front mesh at $t = 0$.

**Table 2 Pearson correlation coefficients for angle-independent strength fields for the isotropic domain**

S_{NH}	S_{NH}	$\bar{S}_N$	$\bar{S}_S$	$\bar{S}_C$	$m(S_N)$	$m(S_S)$	$m(S_C)$
S_{NH}	1	0.917	0.939	0.847	1	1	1
$\bar{S}_N$	0.917	1	0.993	0.950	0.917	0.917	0.917
$\bar{S}_S$	0.939	0.993	1	0.950	0.939	0.939	0.939
$\bar{S}_C$	0.847	0.950	0.950	1	0.847	0.847	0.847
$m(S_N)$	1	0.917	0.939	0.847	1	1	1
$m(S_S)$	1	0.917	0.939	0.847	1	1	1
$m(S_C)$	1	0.917	0.939	0.847	1	1	1

Table 3 Pearson correlation coefficients for angle-independent strength fields for the anisotropic domain

S_{NH}	S_{NH}	$\bar{S}_N$	$\bar{S}_S$	$\bar{S}_C$	$m(S_N)$	$m(S_S)$	$m(S_C)$
S_{NH}	1	0.995	0.993	0.967	1	1	1
$\bar{S}_N$	0.995	1	0.997	0.979	0.995	0.995	0.995
$\bar{S}_S$	0.993	0.997	1	0.990	0.993	0.993	0.993
$\bar{S}_C$	0.967	0.979	0.990	1	0.967	0.967	0.967
$m(S_N)$	1	0.995	0.993	0.967	1	1	1
$m(S_S)$	1	0.995	0.993	0.967	1	1	1
$m(S_C)$	1	0.995	0.993	0.967	1	1	1

4 Conclusion

An upscaling approach was proposed in which an angle-dependent inhomogeneous fracture strength field was
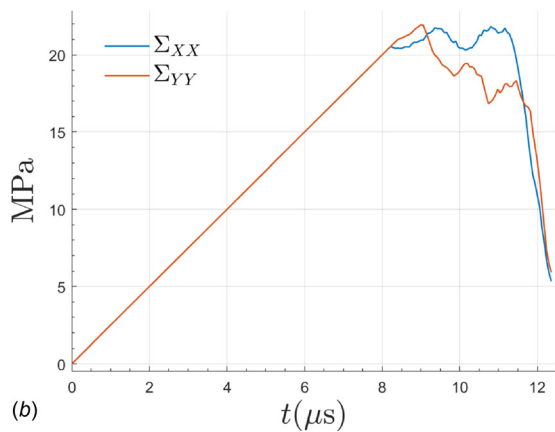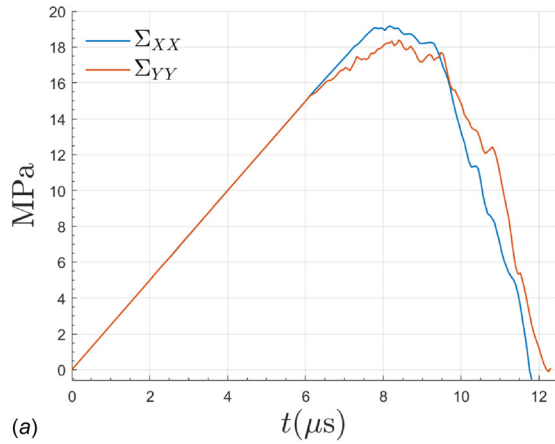
Fig. 18 Macroscopic tensile strain–stress response in *x* and *y* directions: (*a*) isotropic domain and (*b*) anisotropic domain

homogenized from the distribution of cracks at the microscale. The mesoscopic strength field is in turn used for fracture simulations at the macroscale. The computational cost is deemed to be lower compared to direct numerical simulation of the material with explicit representation of its microstructure. The microcrack statistics of a real material, Yuen-Long marble, as described in Ref. [33], was used to generate cracks at the microscale. The proposed multiscale approach can be used to systematically propagate the statistics and randomness of a material at the microscale to uncertainties in its macroscopic failure response.

We use a mixed mode crack propagation criterion, while taking into account the frictional effect for mode *II* fracture, to derive angle-dependent uniaxial tensile, uniaxial compressive, and shear strengths for arbitrary orientations of the loading and a single crack. These strengths are used to derive corresponding angle-dependent strengths for circular SVEs, containing potentially multiple cracks. A 2D macroscopic domain is then traversed with overlapping SVEs in *X* and *Y* directions. The homogenized fracture strengths of each SVE are assigned to its center point. Two rock domains with isotropic and anisotropic distribution of microcracks were homogenized with different SVE sizes. Macroscopic fracture responses were consistent with the underlying statistics of microcracks. For example, for the anisotropic domain, the majority of macroscopic cracks were aligned with the weakest directions of the homogenized mesoscopic strength field.

The pointwise and two-point statistics of the random fields were analyzed. As the SVE size increased, the homogenized field became smoother and higher frequency local variations were lost. This corresponded to lower mean and variation of the homogenized strengths for higher SVE sizes. The spatial covariance function of the strength field was shown to only depend on the distance of two points. The angular covariance function of the
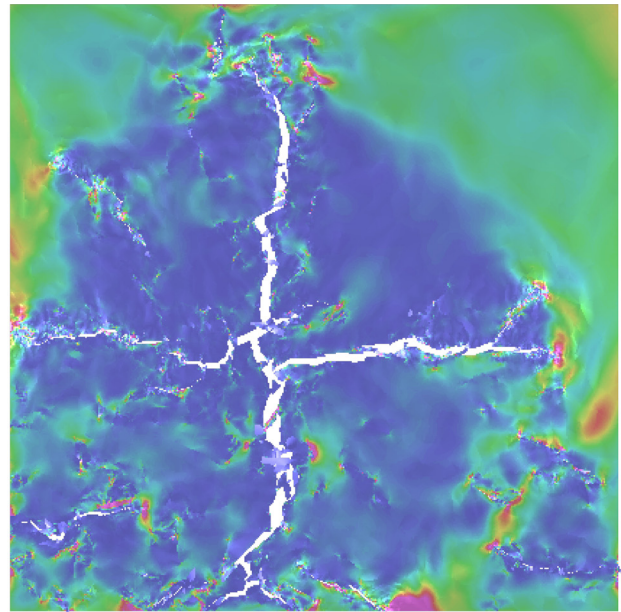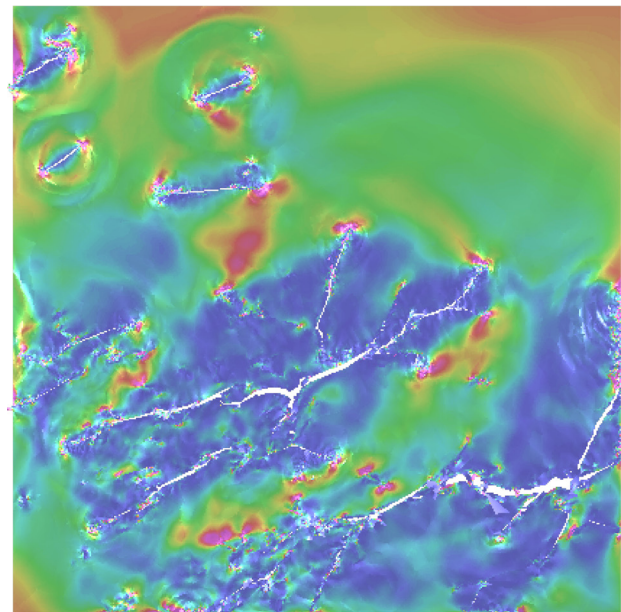

Fig. 19 Strain and kinetic energy densities at *t* = 12 *μ*s: (*a*) Isotropic domain and (*b*) anisotropic domain

isotropic rock should be a function of relative angular distance of two points. In contrast, this function was shown to be much more complex for the anisotropic rock domain.

The effectiveness of this method for homogenization and fracture simulation was demonstrated; however, there are several areas of improvement for future research. First, in this study only fracture properties were assumed to be anisotropic. For more realistic modeling, the elasticity tensor should also be considered inhomogeneous and anisotropic [67], and be homogenized by SVEs. Second, we only presented a single realization of a microcracked domain and its corresponding mesoscopic fracture strength field (for a given SVE size). Many realizations of the microcracked domain (or mesoscopic fracture strength fields) should be generated and analyzed to provide a statistical representation of macroscopic fracture response. Third, the one-point and
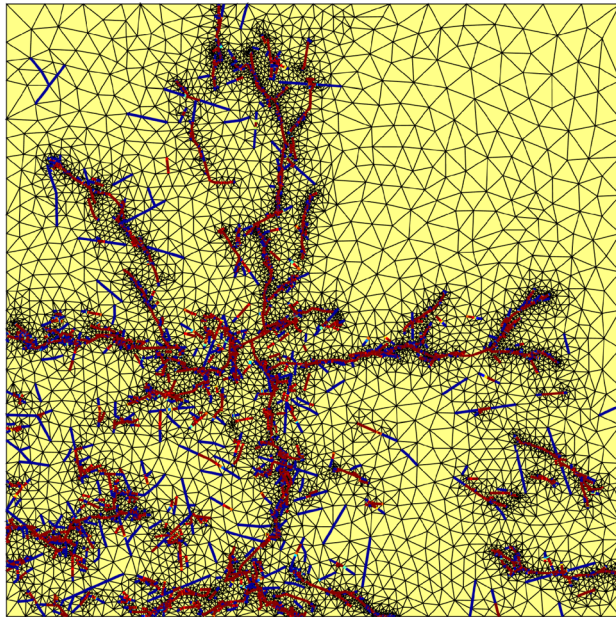
(a)
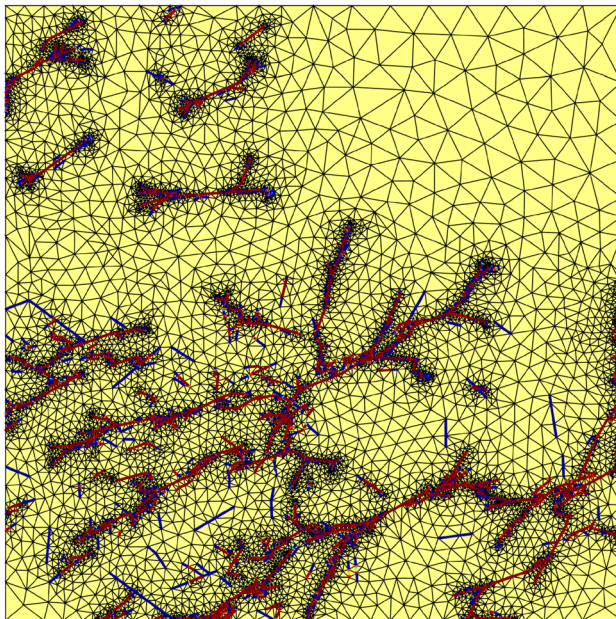
(b)

Fig. 20 aSDG front mesh at $t = 12\ \mu$**s: (**a**) isotropic domain and (**b**) anisotropic domain**

two-point statistics of the mesoscopic random fields, studied here, can be used to circumvent the microscale domain realization and analysis, and directly generate statistically consistent random fields at the mesoscale. Fourth, finite element analysis can be used at the microscale to accurately model microcrack interaction (not modeled in this study) and to calibrate computationally more efficient stochastic bulk damage models [68].

Funding Data

References

[1] Rinaldi, A., Krajcinovic, D., and Mastilovic, S., 2007, "Statistical Damage Mechanics and Extreme Value Theory," Int. J. Damage Mech., **16**(1), pp. 57–76.
[2] Genet, M., Couegnat, G., Tomsia, A., and Ritchie, R., 2014, "Scaling Strength Distributions in Quasi-Brittle Materials From Micro- to Macro-Scales: A Computational Approach to Modeling Nature-Inspired Structural Ceramics," J. Mech. Phys. Solids, **68**(1), pp. 93–106.
[3] Bazant, Z. P., and Le, J.-L., 2017, *Probabilistic Mechanics of Quasibrittle Structures: Strength, Lifetime, and Size Effect*, Cambridge University Press, Cambridge, UK.
[4] Al-Ostaz, A., and Jasiuk, I., 1997, "Crack Initiation and Propagation in Materials With Randomly Distributed Holes," Eng. Fract. Mech., **58**(5–6), pp. 395–420.
[5] Bazant, Z. P., and Planas, J., 1997, *Fracture and Size Effect in Concrete and Other Quasibrittle Materials*, Vol. 16, CRC Press, Boca Raton, FL.
[6] Kozicki, J., and Tejchman, J., 2007, "Effect of Aggregate Structure on Fracture Process in Concrete Using 2D Lattice Model," Arch. Mech., **59**(4–5), pp. 365–84.
[7] Yin, X., Chen, W., To, A., McVeigh, C., and Liu, W., 2008, "Statistical Volume Element Method for Predicting Microstructure-Constitutive Property Relations," Comput. Methods Appl. Mech. Eng., **197**(43–44), pp. 3516–3529.
[8] Li, J., 2000, "Debonding of the Interface as 'Crack Arrestor'," Int. J. Fract., **105**(1), pp. 57–79.
[9] Fascetti, A., Bolander, J. E., and Nisticó, N., 2018, "Lattice Discrete Particle Modeling of Concrete Under Compressive Loading: Multiscale Experimental Approach for Parameter Determination," J. Eng. Mech., **144**(8), p. 04018058.
[10] Weibull, W., 1939, "A Statistical Theory of the Strength of Materials," R. Swed. Inst. Eng. Res., **151**, pp. 1–45.
[11] Weibull, W., 1951, "A Statistical Distribution Function of Wide Applicability," ASME J. Appl. Mech., **18**, pp. 293–297.
[12] Abedi, R., Omidi, O., and Clarke, P., 2016, "Numerical Simulation of Rock Dynamic Fracturing and Failure Including Microscale Material Randomness," 50th U.S. Rock Mechanics/Geomechanics Symposium, Houston, TX, Paper No. ARMA 16–0531.
[13] Abedi, R., Haber, R., and Elbanna, A., 2017, "Mixed-Mode Dynamic Crack Propagation in Rocks With Contact-Separation Mode Transitions," 51th U.S. Rock Mechanics/Geomechanics Symposium, San Francisco, CA, Paper No. ARMA 17–0679.
[14] Abedi, R., Haber, R. B., and Clarke, P. L., 2017, "Effect of Random Defects on Dynamic Fracture in Quasi-Brittle Materials," Int. J. Fract., **208**(1–2), pp. 241–268.
[15] Taylor, L. M., Chen, E.-P., and Kuszmaul, J. S., 1986, "Microcrack-Induced Damage Accumulation in Brittle Rock Under Dynamic Loading," Comput. Methods Appl. Mech. Eng., **55**(3), pp. 301–320.
[16] Homand-Etienne, F., Hoxha, D., and Shao, J., 1998, "A Continuum Damage Constitutive Law for Brittle Rocks," Comput. Geotech., **22**(2), pp. 135–151.
[17] Shao, J., and Rudnicki, J., 2000, "A Microcrack-Based Continuous Damage Model for Brittle Geomaterials," Mech. Mater., **32**(10), pp. 607–619.
[18] Lu, Y., Elsworth, D., and Wang, L., 2013, "Microcrack-Based Coupled Damage and Flow Modeling of Fracturing Evolution in Permeable Brittle Rocks," Comput. Geotech., **49**, pp. 226–44.
[19] Nguyen, V., Stroeven, M., and Sluys, L., 2011, "Multiscale Continuous and Discontinuous Modeling of Heterogeneous Materials: A Review on Recent Developments," J. Multiscale Modell., **03**(4), pp. 229–270.
[20] Ostoja-Starzewski, M., 2002, "Microstructural Randomness Versus Representative Volume Element in Thermomechanics," ASME J. Appl. Mech., **69**(1), pp. 25–35.
[21] Suquet, P., 1997, "Continuum Micromechanics," CISM Courses Lectures, Vol. 272, International Centre for Mechanical Sciences, Udine, Italy.
[22] Kanit, T., Forest, S., Galliet, I., Mounoury, V., and Jeulin, D., 2003, "Determination of the Size of the Representative Volume Element for Random Composites: Statistical and Numerical Approach," Int. J. Solids Struct., **40**(13–14), pp. 3647–79.
[23] Liu, W. K., Siad, L., Tian, R., Lee, S., Lee, D., Yin, X., Chen, W., Chan, S., Olson, G. B., Lindgen, L.-E., Horstemeyer, M. F., Chang, Y.-S., Choi, J.-B., and Kim, Y. J., 2009, "Complexity Science of Multiscale Materials Via Stochastic Computations," Int. J. Numer. Methods Eng., **80**(6–7), pp. 932–978.
[24] Ostoja-Starzewski, M., 2006, "Material Spatial Randomness: From Statistical to Representative Volume Element," Probab. Eng. Mech., **21**(2), pp. 112–132.
[25] Matheron, G., 1989, *Estimating and Choosing. An Essay on Probability on Practice*, Springer, Berlin.
[26] Lantuejoul, C., 1991, "Ergodicity and Integral Range," J. Microsc., **161**(3), pp. 387–403.
[27] Tregger, N., Corr, D., Graham-Brady, L., and Shah, S., 2006, "Modeling the Effect of Mesoscale Randomness on Concrete Fracture," Probab. Eng. Mech., **21**(3), pp. 217–225.
[28] Baxter, S., and Graham, L., 2000, "Characterization of Random Composites Using Moving-Window Technique," J. Eng. Mech., **126**(4), pp. 389–397.
[29] Huyse, L., and Maes, M., 2001, "Random Field Modeling of Elastic Properties Using Homogenization," J. Eng. Mech., **127**(1), pp. 27–36.
[30] Segurado, J., and LLorca, J., 2006, "Computational Micromechanics of Composites: The Effect of Particle Spatial Distribution," Mech. Mater., **38**(8–10), pp. 873–883.
[31] Clarke, P., and Abedi, R., 2017, "Fracture Modeling of Rocks Based on Random Field Generation and Simulation of Inhomogeneous Domains," 51th U.S.

Rock Mechanics/Geomechanics Symposium, San Francisco, CA, June 25–28, Paper No. ARMA 17–0643.

[32] Garrard, J. M., Abedi, R., and Clarke, P. L., 2018, "Modeling of Rock Inhomogeneity and Anisotropy by Explicit and Implicit Representation of Microcracks," 52nd U.S. Rock Mechanics/Geomechanics Symposium, Seattle, WA, June 17–20, Paper No. ARMA 18-151-0228-1094.

[33] Wong, T.-F., Wong, R. H., Chau, K., and Tang, C., 2006, "Microcrack Statistics, Weibull Distribution and Micromechanical Modeling of Compressive Failure in Rock," Mech. Mater., 38(7), pp. 664–681.

[34] Garrard, J. M., Abedi, R., and Clarke, P. L., 2018, "Statistical Volume Elements for the Characterization of Angle-Dependent Fracture Strengths," ASME Paper No. IMECE2018-88257.

[35] Pietruszczak, S., and Mroz, Z., 2000, "Formulation of Anisotropic Failure Criteria Incorporating a Microstructure Tensor," Comput. Geotech., 26(2), pp. 105–112.

[36] Pietruszczak, S., Lydzba, D., and Shao, J., 2002, "Modelling of Inherent Anisotropy in Sedimentary Rocks," Int. J. Solids Struct., 39(3), pp. 637–648.

[37] Hoek, E., and Brown, E. T., 1980, Underground Excavations in Rock, CRC Press, Boca Raton, FL.

[38] Pietruszczak, S., and Mroz, Z., 2001, "On Failure Criteria for Anisotropic Cohesive-Frictional Materials," Int. J. Numer. Anal. Methods Geomech., 25(5), pp. 509–524.

[39] Lee, Y.-K., and Pietruszczak, S., 2008, "Application of Critical Plane Approach to the Prediction of Strength Anisotropy in Transversely Isotropic Rock Masses," Int. J. Rock Mech. Min. Sci., 45(4), pp. 513–523.

[40] Shi, X., Yang, X., Meng, Y., and Li, G., 2016, "An Anisotropic Strength Model for Layered Rocks Considering Planes of Weakness," Rock Mech. Rock Eng., 49(9), pp. 3783–92.

[41] Abedi, R., Haber, R. B., and Petracovici, B., 2006, "A Spacetime Discontinuous Galerkin Method for Elastodynamics With Element-Level Balance of Linear Momentum," Comput. Methods Appl. Mech. Eng., 195(25–28), pp. 3247–3273.

[42] Dowd, P., Xu, C., Mardia, K., and Fowell, R., 2007, "A Comparison of Methods for the Stochastic Simulation of Rock Fractures," Math. Geol., 39(7), pp. 697–714.

[43] Renshaw, C. E., 1999, "Connectivity of Joint Networks With Power Law Length Distributions," Water Resour. Res., 35(9), pp. 2661–2670.

[44] Garrard, J. M., and Abedi, R., 2019, "Statistical Volume Element Averaging Scheme for Fracture of Quasibrittle Materials," Comput. Geotech. (accepted).

[45] Erdogan, F., and Sih, G., 1963, "On the Crack Extension in Plates Under Plane Loading and Transverse Shear," ASME J. Basic Eng., 85(4), pp. 519–525.

[46] Hussain, M., Pu, S., and Underwood, J., 1974, "Strain Energy Release Rate for a Crack Under Combined Mode I and Mode II," Fracture Analysis: 1973 National Symposium on Fracture Mechanics, In Part II, ASTM International, College Park, MD, pp. 2–28.

[47] Anderson, T. L., 2017, Fracture Mechanics: Fundamentals and Applications, CRC Press, New York.

[48] Ashby, M., and Hallam, S., 1986, "The Failure of Brittle Solids Containing Small Cracks Under Compressive Stress States," Acta Metall., 34(3), pp. 497–510.

[49] Matheron, G., 1971, The Theory of Regionalized Variables and Its Applications, Paris School of Mines Publications, Paris, France.

[50] Neuman, S. P., Riva, M., and Guadagnini, A., 2008, "On the Geostatistical Characterization of Hierarchical Media," Water Resour. Res., 44(2), p. W02403.

[51] Abedi, R., Chung, S.-H., Erickson, J., Fan, Y., Garland, M., Guoy, D., Haber, R., Sullivan, J. M., Thite, S., and Zhou, Y., 2004, "Spacetime Meshing With Adaptive Refinement and Coarsening," 20th Annual Symposium on Computational Geometry (SCG '04), ACM, Brooklyn, NY, June 8–11, pp. 300–309.

[52] Abedi, R., and Clarke, P. L., 2019, "A Computational Approach to Model Dynamic Contact and Fracture Mode Transitions in Rock," Comput. Geotech., 109, pp. 248–271.

[53] Camacho, G. T., and Ortiz, M., 1996, "Computational Modelling of Impact Damage in Brittle Materials," Int. J. Solids Struct., 33(20–22), pp. 2899–2938.

[54] Abedi, R., Hawker, M. A., Haber, R. B., and Matouš, K., 2009, "An Adaptive Spacetime Discontinuous Galerkin Method for Cohesive Models of Elastodynamic Fracture," Int. J. Numer. Methods Eng., 1, pp. 1–42.

[55] Abedi, R., Haber, R. B., Thite, S., and Erickson, J., 2006, "An h–Adaptive Spacetime–Discontinuous Galerkin Method for Linearized Elastodynamics," Revue Européenne de Mécanique Numérique (Eur. J. Comput. Mech.), 15(6), pp. 619–642.

[56] Abedi, R., Omidi, O., and Enayatpour, S., 2018, "A Mesh Adaptive Method for Dynamic Well Stimulation," Comput. Geotech., 102, pp. 12–27.

[57] Belytschko, T., and Black, T., 1999, "Elastic Crack Growth in Finite Elements With Minimal Remeshing," Int. J. Numer. Methods Eng., 45(5), pp. 601–620.

[58] Moës, N., Dolbow, J., and Belytschko, T., 1999, "A Finite Element Method for Crack Growth Without Remeshing," Int. J. Numer. Methods Eng., 46(1), pp. 131–150.

[59] Duarte, C. A., Babuška, I., and Oden, T. J., 2000, "Generalized Finite Element Methods for Three-Dimensional Structural Mechanics," Comput. Struct., 77(2), pp. 215–232.

[60] Strouboulis, T., Babuska, I., and Copps, K., 2000, "The Design and Analysis of the Generalized Finite Element Method," Comput. Methods Appl. Mech. Eng., 181(1–3), pp. 43–69.

[61] Abedi, R., and Haber, R. B., 2018, "Spacetime Simulation of Dynamic Fracture With Crack Closure and Frictional Sliding," Adv. Model. Simul. Eng. Sci., 5(1), p. 22.

[62] Acton, K. A., Baxter, S. C., Bahmani, B., Clarke, P. L., and Abedi, R., 2018, "Voronoi Tessellation Based Statistical Volume Element Characterization for Use in Fracture Modeling," Comput. Methods Appl. Mech. Eng., 336, pp. 135–155.

[63] Bahmani, B., Yang, M., Nagarajan, A., Clarke, P. L., Soghrati, S., and Abedi, R., 2019, "Automated Homogenization-Based Fracture Analysis: Effects of SVE Size and Boundary Condition," Comput. Methods Appl. Mech. Eng., 345, pp. 701–727.

[64] Karhunen, K., and Selin, I., 1960, On Linear Methods in Probability Theory, Rand Corporation, Santa Monica, CA.

[65] Loéve, M., 1977, Probability Theory, Springer, New York.

[66] Nemat-Nasser, S., and Hori, M., 1993, Micromechanics: Overall Properties of Heterogeneous Materials, Elsevier, Amsterdam; New York.

[67] Staber, B., and Guilleminot, J., 2017, "Stochastic Modeling and Generation of Random Fields of Elasticity Tensors: A Unified Information-Theoretic Approach," C. R. Méc., 345(6), pp. 399–416.

[68] Malyarenko, A., and Ostoja-Starzewski, M., 2019, "Towards Stochastic Continuum Damage Mechanics," Int. J. Solids Struct. (in press).